



Comparison of Theoretical and Experimental Unsteady Aerodynamics of Linear Oscillating Cascade With Supersonic Leading-Edge Locus

John K. Ramsey
Glenn Research Center, Cleveland, Ohio

Dan Erwin
Ohio State University, Columbus, Ohio

The NASA STI Program Office . . . in Profile

Since its founding, NASA has been dedicated to the advancement of aeronautics and space science. The NASA Scientific and Technical Information (STI) Program Office plays a key part in helping NASA maintain this important role.

The NASA STI Program Office is operated by Langley Research Center, the Lead Center for NASA's scientific and technical information. The NASA STI Program Office provides access to the NASA STI Database, the largest collection of aeronautical and space science STI in the world. The Program Office is also NASA's institutional mechanism for disseminating the results of its research and development activities. These results are published by NASA in the NASA STI Report Series, which includes the following report types:

- **TECHNICAL PUBLICATION.** Reports of completed research or a major significant phase of research that present the results of NASA programs and include extensive data or theoretical analysis. Includes compilations of significant scientific and technical data and information deemed to be of continuing reference value. NASA's counterpart of peer-reviewed formal professional papers but has less stringent limitations on manuscript length and extent of graphic presentations.
- **TECHNICAL MEMORANDUM.** Scientific and technical findings that are preliminary or of specialized interest, e.g., quick release reports, working papers, and bibliographies that contain minimal annotation. Does not contain extensive analysis.
- **CONTRACTOR REPORT.** Scientific and technical findings by NASA-sponsored contractors and grantees.

- **CONFERENCE PUBLICATION.** Collected papers from scientific and technical conferences, symposia, seminars, or other meetings sponsored or cosponsored by NASA.
- **SPECIAL PUBLICATION.** Scientific, technical, or historical information from NASA programs, projects, and missions, often concerned with subjects having substantial public interest.
- **TECHNICAL TRANSLATION.** English-language translations of foreign scientific and technical material pertinent to NASA's mission.

Specialized services that complement the STI Program Office's diverse offerings include creating custom thesauri, building customized databases, organizing and publishing research results . . . even providing videos.

For more information about the NASA STI Program Office, see the following:

- Access the NASA STI Program Home Page at <http://www.sti.nasa.gov>
- E-mail your question via the Internet to help@sti.nasa.gov
- Fax your question to the NASA Access Help Desk at 301-621-0134
- Telephone the NASA Access Help Desk at 301-621-0390
- Write to:
NASA Access Help Desk
NASA Center for Aerospace Information
7121 Standard Drive
Hanover, MD 21076

NASA/TM—2004-211820



Comparison of Theoretical and Experimental Unsteady Aerodynamics of Linear Oscillating Cascade With Supersonic Leading-Edge Locus

John K. Ramsey
Glenn Research Center, Cleveland, Ohio

Dan Erwin
Ohio State University, Columbus, Ohio

National Aeronautics and
Space Administration

Glenn Research Center

June 2004

Acknowledgments

The authors appreciate the contributions from the following persons without whom this project would not have been possible: Dr. Marvin Goldstein and the Research Advisory Board for realizing the importance of this experimental research and funding this project; Dr. Dan Buffum, who provided the essential data reduction software; Dr. Larry Bober and Dr. Dan Hoyniak for their valuable inputs; Dennis Huff and Dr. T.S. Reddy for their Euler analysis; Dr. Stephen Whitmore for his CFD analysis to determine phase lag and pressure errors due to the pressure transducer orifice geometry; Al Buggele for his valuable consultation on the oscillating drive mechanism; Dr. Don Braun for his valuable assistance in data reduction; Erwin Meyn for his consultation on data acquisition; Phylis Sramek for drafting; Richard Meden for airfoil fabrication; Steve Cobb and Ed Ramsey of Steve Cobb's Weidner Motors (Mansfield, Ohio) for providing the tachometer; and Sergeant Terry Potter and the Army National Guard (Newark, Ohio) for calibrating the gunners sight. The authors also appreciate the contributions from the following persons at The Ohio State University's Aeronautical and Astronautical Research Laboratory, who played a vital role in making this project a reality: Dr. John D. Lee for the design of the nozzle blocks; Dr. Gerald Gregorek for his valuable consultations; Tom Veit, Carl Kipp, and Mike McKee for fabricating the oscillating cascade facility; Doug Campbell, Mike Hoffman, and Dr. Rick Freuler for electronics, data acquisition, and computer support; Jeff Keip for computer software support; and Floyd Rister for wind tunnel operation. The wind tunnel test section, airfoils, and oscillating mechanism were designed and fabricated and the unsteady experimental influence coefficients acquired within 2 years. From the standpoint of limited funding support and time constraints, this was a high-risk endeavor. It was only with God's Providence that the successes of this work were made possible.

The CD in the back of this report contains a PDF file of this report with links to view the movie along with the movie file of a typical wind tunnel run with an oscillating mechanism. Links to view the movie can also be found in figures 4 and 8 in the online PDF version.

Note that at the time of research, the NASA Lewis Research Center was undergoing a name change to the NASA John H. Glenn Research Center at Lewis Field. Both names may appear in this report.

Trade names or manufacturers' names are used in this report for identification only. This usage does not constitute an official endorsement, either expressed or implied, by the National Aeronautics and Space Administration.

Available from

NASA Center for Aerospace Information
7121 Standard Drive
Hanover, MD 21076

National Technical Information Service
5285 Port Royal Road
Springfield, VA 22100

Available electronically at <http://gltrs.grc.nasa.gov>

Comparison of Theoretical and Experimental Unsteady Aerodynamics of Linear Oscillating Cascade With Supersonic Leading-Edge Locus

John K. Ramsey
National Aeronautics and Space Administration
Glenn Research Center
Cleveland, Ohio 44135

Dan Erwin
Ohio State University
Columbus, Ohio 43210

Summary

An experimental influence coefficient technique was used to obtain unsteady aerodynamic influence coefficients and, consequently, unsteady pressures for a cascade of symmetric airfoils oscillating in pitch about midchord. Stagger angles of 0° and 10° were investigated for a cascade with a gap-to-chord ratio of 0.417 operating at an axial Mach number of 1.9, resulting in a supersonic leading-edge locus. Reduced frequencies ranged from 0.056 to 0.2. The influence coefficients obtained determine the unsteady pressures for any interblade phase angle. The unsteady pressures were compared with those predicted by several algorithms for interblade phase angles of 0° and 180° .

1.0 Introduction

This report represents a research effort carried out nearly a decade ago when the NASA Lewis Research Center (now the NASA Glenn Research Center) was developing propulsion technology in support of the supersonic throughflow fan (SSTF) engine. A detailed description of this engine and its benefits, as well as associated research, is given in references 1 and 2. A unique characteristic of the SSTF is that the rotor operates in supersonic axial flow and hence all rotor blade bow shocks exist downstream of the locus of blade leading edges. A rotor with this flow configuration is characterized as having a supersonic leading-edge locus (SLEL). Experimental research on the SSTF concept prior to the work performed at NASA Lewis was extremely limited (refs. 3 to 5). Therefore, a research effort was begun to evaluate the concept and potential of the SSTF engine (refs. 6 and 7). During the initial design of the SSTF rotor, aeroelastic stability became a concern. Consequently, a computer algorithm (ref. 8) was developed to determine the aeroelastic stability of the SSTF. This algorithm is based on Lane's (ref. 9) unsteady aerodynamic theory for an oscillating cascade of flat plates with an SLEL. The algorithm was incorporated into an existing aeroelastic code (ref. 10) for use in determining the aeroelastic stability of the SSTF rotor (ref. 11).

In an effort to improve on the aeroelastic analysis capabilities while still providing for efficient analysis turnaround time, the algorithm based on Lane's theory was modified to include the effects of thickness and camber in the noninterference regions of a cascade with an SLEL (refs. 12 and 13). In addition, computational fluid dynamic (CFD) codes were being developed to predict the unsteady lift and moment coefficients necessary for determining aeroelastic stability (refs. 14 to 18). The desire to correlate the codes with experimental data resulted in an experimental effort to measure unsteady

pressures on an oscillating cascade with an SLEL. This effort was first described in references 19 and 20. This report compares the experimental data with values predicted by the algorithms of references 8, 12, and 18.

Experimental unsteady pressure data are presented for a linear cascade of airfoils with an SLEL oscillating (with amplitudes of 1.2° about 0° angle of attack) in pitch about midchord having a gap-to-chord ratio of 0.417 and stagger angles of 0° and 10° . Experimental influence coefficients were obtained that determine unsteady pressures for any interblade phase angle. Specifically, unsteady pressure coefficients for interblade phase angles of 0° and 180° were determined from the experimental influence coefficients.

The influence coefficient technique used to acquire the unsteady pressure data is described next, and then the experimental facility and the data acquisition and reduction techniques. Experimental results for stagger angles of 0° and 10° and for interblade phase angles of 0° and 180° are then presented. Although a stagger angle of 0° would not typically simulate an actual turbomachinery situation, it nonetheless simplifies the experimental process (as made clear subsequently) and at the same time provides experimental data for correlation purposes.

2.0 Influence Coefficient Technique

2.1 Preliminaries

A linear influence coefficient technique based on the work of reference 21 was used to compute the unsteady pressure distribution on the oscillating cascade. This technique determines unsteady pressure coefficients C_p for any interblade phase angle β . The complex-valued unsteady pressure coefficient is defined as

$$C_p = \frac{P_1}{q_\infty \alpha_1} \quad (1)$$

where P_1 is the complex-valued first harmonic of the airfoil surface static pressure, q_∞ is the free-stream dynamic pressure, and α_1 is the amplitude of airfoil oscillation (radians). All symbols are defined in appendix A.

For a finite cascade of $2N + 1$ airfoils executing constant harmonic oscillations with a constant interblade phase angle β , the unsteady pressure coefficient $C_{p_{u,l}}$ can be expressed as a Fourier series of complex-valued unsteady aerodynamic influence coefficients $\bar{C}_{p_{u,l}}^n$ (ref. 21)

$$C_{p_{u,l}}(x, \beta) = \sum_{n=-N}^N \bar{C}_{p_{u,l}}^n(x) e^{in\beta} \quad (2)$$

The superscript is the index number of the airfoil that is oscillating, and the subscripts u and l refer to the upper (suction) and lower (pressure) surfaces of the reference airfoil ($n = 0$), respectively.

Figure 1 illustrates a cascade of airfoils. In a cascade of airfoils with an SLEL, each interblade passage is aerodynamically isolated from all other interblade passages. Therefore, in addition to the reference airfoil ($n = 0$), only the two airfoils $n = -1, 1$ that bound the reference airfoil contribute to the unsteady pressures on the reference airfoil. In other words, only airfoils with indices $n = -1, 0, 1$

contribute to the unsteady pressure on the reference airfoil. More specifically, both surfaces of the reference airfoil ($n = 0$), the lower surface of the upper airfoil ($n = 1$), and the upper surface of the lower airfoil ($n = -1$) contribute to the unsteady pressure coefficients on the reference airfoil. Therefore, equation (2) becomes

$$C_{p_{u,l}}(x, \beta) = \sum_{n=-1}^1 \bar{C}_{p_{u,l}}^n(x) e^{in\beta} \quad (3)$$

Figure 2 illustrates a cascade of airfoils with an SLEL. Portions of each airfoil surface are isolated from any aerodynamic influences originating from neighboring airfoils. These surfaces are denoted as noninterference surfaces. In particular, the unsteady pressure distribution on the noninterference surfaces of the reference airfoil are not influenced by the presence of airfoils $n = -1, 1$. Therefore, the unsteady pressures on these surface regions of the reference airfoil are not influenced by interblade phase angles. All influence coefficients on the noninterference airfoil regions are null except for the influence coefficient due to the motion of the reference airfoil itself. Thus,

$$\bar{C}_{p_{u,l}}^n(x, \beta) = 0 \quad n \neq 0 \quad x < x_s^{u,l} \quad (4)$$

where x_s^u and x_s^l are the shock impingement locations on the upper and lower surfaces of the reference airfoil, respectively (see fig. 2).

The unsteady pressure coefficients upstream of the first shock wave impingement location for the upper and lower reference airfoil surfaces are

$$C_{p_u}(x, \beta) = \bar{C}_{p_u}^0 \quad x < x_s^u \quad (5)$$

and

$$C_{p_l}(x, \beta) = \bar{C}_{p_l}^0 \quad x < x_s^l \quad (6)$$

respectively. The unsteady pressure coefficients downstream of the first shock wave impingement location for the upper and lower reference airfoil surfaces are

$$C_{p_u}(x, \beta) = \bar{C}_{p_u}^0 + \bar{C}_{p_u}^1 e^{i\beta} \quad x \geq x_s^u \quad (7)$$

and

$$C_{p_l}(x, \beta) = \bar{C}_{p_l}^0 + \bar{C}_{p_l}^{-1} e^{-i\beta} \quad x \geq x_s^l \quad (8)$$

respectively.

Equations (5) to (8) may be combined by introducing the asymmetrical unit step function defined as (ref. 22)

$$U_-(x - x_s) = \begin{cases} 0 & x < x_s \\ 1 & x \geq x_s \end{cases} \quad (9)$$

Combining equations (5) and (7) and incorporating equation (9) yield

$$C_{p_u}(x, \beta) = \bar{C}_{p_u}^0 + \bar{C}_{p_u}^1 e^{i\beta} U_-(x - x_s^u) \quad (10)$$

Also combining equations (6) and (8) and using equation (9) give

$$C_{p_l}(x, \beta) = \bar{C}_{p_l}^0 + \bar{C}_{p_l}^{-1} e^{-i\beta} U_-(x - x_s^l) \quad (11)$$

Equations (10) and (11) can be used to determine the unsteady pressure and consequently the unsteady lift and moment coefficients for a cascade with an SLEL.

The two-dimensional unsteady lift and moment coefficients are defined as

$$c_l = c \int_0^1 \Delta C_p d \frac{x}{c} \quad (12)$$

and

$$c_m = c^2 \int_0^1 \Delta C_p \left(\frac{x}{c} - \frac{x_0}{c} \right) d \frac{x}{c} \quad (13)$$

respectively, where c is the airfoil chord and x is the streamwise coordinate. The unsteady pressure difference coefficient ΔC_p for the reference airfoil is defined as

$$\Delta C_p = C_{p_l} - C_{p_u} \quad (14)$$

Upon substitution of equations (10) and (11) into equation (14) the unsteady pressure difference coefficient becomes

$$\Delta C_p = \bar{C}_{p_l}^0 + \bar{C}_{p_l}^{-1} e^{-i\beta} U_-(x - x_s^l) - \bar{C}_{p_u}^0 - \bar{C}_{p_u}^1 e^{i\beta} U_-(x - x_s^u) \quad (15)$$

2.2 Techniques

Figure 3 shows five techniques or scenarios for measuring the unsteady pressure influence coefficients by using a cascade of two or three airfoils. The first technique is accomplished in three steps (fig. 3(a)). It uses three airfoils in the first step with only two airfoils required in the second and third steps. In each step a different airfoil is oscillated while unsteady pressures are measured on the reference airfoil. The reference airfoil is instrumented on both its upper and lower surfaces and remains in the middle location of the cascade for each step. The airfoil oscillation system for this technique must be able to oscillate an airfoil in each of the three different airfoil locations within the cascade.

The second technique (fig. 3(b)) uses three airfoils in the first step, with only two airfoils required in the remaining steps, just as for the technique described above. The reference airfoil is instrumented on both its upper and lower surfaces and is located in a different position in the cascade for each step. However, unlike the first approach the middle airfoil is oscillated in each step while unsteady pressures are measured on the reference airfoil, which is in a different location for each step. The airfoil oscillation system for this technique need only oscillate the airfoil in the middle location of the cascade.

For symmetric airfoils the technique illustrated in figure 3(c) may be used and was the method employed in this work. This technique uses a cascade of two monoconvex airfoils instrumented on their convex surfaces. It requires two steps, each with equal and opposite stagger angle. This technique will work for nonsymmetric airfoils, where one airfoil is instrumented on its pressure (lower) surface and the other airfoil is instrumented on its suction (upper) surface. Nonsymmetric airfoils must be inverted in step 2 as indicated by the coordinate system orientation and must be switched in location as well. The airfoil oscillation system for this technique need only oscillate the lower airfoil of the cascade. This technique will be described in detail shortly, but for now two additional techniques are presented.

Figure 3(d) illustrates an additional technique using a two-airfoil cascade. This technique consists of four steps and uses both positive and negative stagger. One airfoil is instrumented on both surfaces. In each step the lower airfoil in the cascade is oscillated. The instrumented airfoil is in a different position in the cascade from step to step. For symmetric airfoils this technique can use monoconvex airfoils, with their convex surfaces facing each other. Nonsymmetric airfoils must be inverted in steps 3 and 4 as indicated by the respective coordinate system orientations. The disadvantage of this approach is the need to perform four wind tunnel runs.

Finally, figure 3(e) presents a technique using three airfoils. The middle airfoil in the cascade is instrumented on both surfaces. The upper and lower airfoils are instrumented on their lower and upper surfaces, respectively. All influence coefficients are obtained from the four instrumented surfaces in one step wherein the middle airfoil is oscillated.

As already stated, the technique illustrated in figure 3(c) was used in this work and is denoted as the two-airfoil technique. This novel technique has several advantages over the others presented. The two-airfoil technique requires only two steps, as opposed to the three steps required for the techniques illustrated in figures 3(a) and (b) and the four steps required for that illustrated in figure 3(d). Although only one step is required for the technique illustrated in figure 3(e), the disadvantage of this approach is the need to instrument four surfaces and the resulting increase in data acquisition efforts to sample all four surfaces simultaneously.

Although not used in this work, the three-airfoil technique illustrated in figure 3(a) is presented next to facilitate a better understanding of the two-airfoil technique, which will be presented subsequently.

2.2.1 Three-airfoil technique (one instrumented airfoil).—With the upper and lower surfaces of the reference airfoil instrumented (see fig. 3(a)), all coefficients corresponding to a given Mach number, reduced frequency, and stagger angle can be obtained in three steps as follows:

1. Oscillate the reference airfoil ($n = 0$) and measure the unsteady pressure on the reference airfoil to obtain $\bar{C}_{p_u}^0$ and $\bar{C}_{p_l}^0$ as shown in step 1 of figure 3(a).
2. Oscillate the lower airfoil ($n = -1$) and measure the unsteady pressure on the lower surface of the reference airfoil to get $\bar{C}_{p_l}^{-1}$ as shown in step 2 of figure 3(a).
3. Oscillate the upper airfoil ($n = 1$) and measure the unsteady pressure on the upper surface of the reference airfoil to get $\bar{C}_{p_u}^1$ as shown in step 3 of figure 3(a).

2.2.2 Two-airfoil technique (two instrumented airfoils).—In order to acquire the four influence coefficients for a cascade with stagger, two steps are necessary as shown in figure 3(c). Each step would normally correspond to a separate wind tunnel run: one run with the airfoils at positive stagger and the other with the airfoils at an equal negative stagger (fig. 3(c)). The reduced frequency must be the same for both wind tunnel runs. For a case with stagger all steps may be accomplished in one wind tunnel run if some mechanical arrangement is used to automatically adjust from positive to negative stagger during the same wind tunnel run. For the case of 0° stagger angle, only one wind tunnel run is necessary, as discussed in section 2.2.3.

In the two-airfoil technique two airfoils are instrumented on their convex surfaces. The lower and upper airfoils are designated as airfoils A and B, respectively. Influence coefficients are acquired for a cascade with stagger in the following manner:

1. With the airfoils at positive stagger as shown in step 1 of figure 3(c), airfoil A is oscillated. As shown, influence coefficients $\bar{C}_{p_u}^0$ and $\bar{C}_{p_l}^{-1}$ are obtained in the same wind tunnel run. Airfoil A simultaneously simulates the reference airfoil and the lower airfoil ($n = -1$) of the three-airfoil technique as shown in steps 1 and 2 of figure 3(a). Airfoil B simultaneously simulates the upper airfoil ($n = 1$) and the reference airfoil of the three-airfoil technique as shown in steps 1 and 2 of figure 3(a).
2. With the airfoils at negative stagger as shown in step 2 of figure 3(c), airfoil A is oscillated again. Influence coefficients $\bar{C}_{p_u}^1$ and $\bar{C}_{p_l}^0$ are obtained. Airfoils A and B simulate the upper airfoil ($n = 1$) and the reference airfoil, respectively, of the three-airfoil technique as shown in step 3 of figure 3(a). In this case the pitch-up (clockwise rotation) of airfoil A in step 2 (fig. 3(c)) represents a pitch-down (counterclockwise rotation) of airfoil 1 in the three-airfoil technique (fig. 3(a)).

2.2.3 Two-airfoil technique (zero stagger angle).—When the two-airfoil cascade has 0° stagger angle, equation (15) can be further simplified. At 0° stagger angle the shock wave impingements are at the same x/c locations for the upper and lower surfaces of airfoils A and B (generally only true for symmetric airfoils or, in this case, monoconvex airfoils with their convex portions facing each other). Hence,

$$x_s^u = x_s^l = x_s \quad (16)$$

A pitch-up (clockwise rotation) of airfoil A in step 1 of figure 3(c) corresponds to a pitch-down (counterclockwise rotation) of airfoil A in step 2 of figure 3(c). Thus, the motion of airfoil A in step 1 of figure 3(c) is 180° out of phase with the motion of airfoil A in step 2 of figure 3(c), from the viewpoint of the cascade coordinate systems shown. Because all influence coefficients are acquired with respect to the oscillatory motion of airfoil A, it is evident that $\bar{C}_{p_l}^{-1}$ will be 180° out of phase with respect to $\bar{C}_{p_u}^1$. However, their magnitudes will be equal. For this case of 0° stagger, coefficients $\bar{C}_{p_l}^{-1}$ and $\bar{C}_{p_u}^1$ are measured on airfoil B in the same wind tunnel run. Therefore,

$$\bar{C}_{p_l}^{-1} = \bar{C}_{p_u}^1 e^{i\pi} = -\bar{C}_{p_u}^1 \quad (17)$$

Likewise, coefficients $\bar{C}_{p_u}^0$ and $\bar{C}_{p_l}^0$ are measured on airfoil A in the same wind tunnel run. It can also be seen from steps 1 and 2 of figure 3(c) that coefficients $\bar{C}_{p_u}^0$ and $\bar{C}_{p_l}^0$ are 180° out of phase and have the same magnitudes. Therefore,

$$\bar{C}_{p_u}^0 = \bar{C}_{p_l}^0 e^{i\pi} = -\bar{C}_{p_l}^0 \quad (18)$$

Substituting equations (16) to (18) into equation (15) yields

$$\Delta C_p = 2\bar{C}_{p_l}^0 - \bar{C}_{p_u}^1 \left(e^{-i\beta} + e^{i\beta} \right) U_-(x - x_s) \quad (19)$$

Let \bar{C}_{p_A} and \bar{C}_{p_B} represent the influence coefficients measured at 0° stagger angle on airfoils A and B, respectively, resulting in

$$\bar{C}_{p_A} = \bar{C}_{p_u}^0 = \bar{C}_{p_l}^0 e^{i\pi} = -\bar{C}_{p_l}^0 \quad (20)$$

and

$$\bar{C}_{p_B} = \bar{C}_{p_l}^{-1} = \bar{C}_{p_u}^1 e^{i\pi} = -\bar{C}_{p_u}^1 \quad (21)$$

Substituting equations (20) and (21) into equation (19) gives

$$\Delta C_p = -2\bar{C}_{p_A} + \bar{C}_{p_B} \left(e^{-i\beta} + e^{i\beta} \right) U_-(x - x_s) \quad (22)$$

Equation (22) can be used to calculate the unsteady pressure difference coefficient for a cascade of symmetric airfoils with an SLEL having a 0° stagger angle.

3.0 Experimental Facility

3.1 Wind Tunnel

The experimental oscillating cascade facility (OCF) used to obtain the unsteady pressures was conceived as a modification to the existing Ohio State University Aeronautical and Astronautical Research Laboratory's high-Reynolds-number blowdown wind tunnel. The modification consisted of replacing the transonic tunnel section with a supersonic tunnel section. The OCF (fig. 4) consists of a settling chamber, a supersonic tunnel section, an exhaust pipe, and an oscillating mechanism. The complete oscillating mechanism is not shown in figure 4. The settling chamber is approximately 10 ft long and 3 ft in diameter. The tunnel is 58 in. long with a constant-area test section 6 in. wide by 12 in. high.

Referring to figure 4, the dry air enters the dual-can squirter and is diffused radially as it enters the settling chamber. The dual-can squirter consists of two concentrically mounted cans with solid downstream ends and porous sides. Upon entering the settling chamber the airflow then travels through a porous plate and through a section of 9-in.-long honeycomb. The honeycomb straightens the airflow by removing radial velocity components. After leaving the honeycomb flow straightener the air passes through three screens which dampen any remaining turbulence in the flow. After passing through the last settling chamber screen the flow then enters the convergent portion of the wind tunnel, passes through the throat, and is expanded to supersonic flow in the test section. The flow exits the facility through a circular pipe and is exhausted into the atmosphere.

Figure 5 shows a schematic diagram of the air supply system for the blowdown OCF. Two storage tanks provide 1500 ft^3 of dry air at 2400 psi. The air is compressed and pumped through an air dryer into the tanks by two four-stage compressors. A central valve system controls the airflow to the OCF. The air is admitted to the stagnation/settling chamber by opening a 1/4-turn plug valve. The flow rate is set by a cone valve. A manually operated butterfly valve connects the OCF to the high-pressure air supply.

Figure 6 shows the aluminum wind tunnel section with the north side wall and north nozzle block removed. The tunnel sides consist of the nozzle blocks (fig. 7) and the side walls. The roof and floor are each one contiguous piece as shown in figure 6. Fasteners join the nozzle blocks and side walls to the roof and floor. The exhaust flange (fig. 6) connects the tunnel to the exhaust pipe. The airfoil windows mount in the nozzle blocks as shown in figures 6 and 7. The windows may be rotated in the nozzle

blocks, positioning the upper airfoil either upstream, downstream, or directly above the lower airfoil and thus providing various stagger angles. The window angular orientation and thus cascade stagger angle was determined by measuring the inclination from horizontal of a flat plate placed on two dowels extending outward from the window as shown in figure 8. The windows were secured in place by using four toe clamps also shown in figure 8.

3.2 Airfoils

Figure 9 shows one of the two airfoils that compose the supersonic cascade. The airfoils are monoconvex with an instrumentation cover machined into the outer surface (away from the cascade passage) as shown in figure 10. Figure 11 shows the airfoil with the instrumentation cover installed. Figure 12 shows the cascade with one nozzle block removed. The airfoils were machined from 17-4PH stainless steel and heat treated to improve fracture toughness. A circular trunnion at each spanwise end of the airfoils was followed by a rectangular boss. The circular trunnion fit into a sintered bronze bushing mounted in the tunnel window. This trunnion supported the aerodynamic loading while allowing angle of attack orientation and/or oscillatory motion of the airfoil. The boss on the south end of the lower airfoil (airfoil A) provided the attachment point for the oscillating mechanism, while the boss on the north end provided a reference surface for angle-of-attack alignment. The bosses on each end of the upper airfoil (airfoil B) provided an attachment point to clamp the airfoil to the window (see fig. 8) at a fixed 0° angle of attack. The radius of the convex surface was 19.8 in. and the airfoil span was nominally 5.97 in., providing a 0.015-in. gap between each airfoil end and the test section window/side wall. The gap provided space for installing off-the-shelf felt pads with adhesive backing. One felt pad was placed upstream and one downstream of the trunnion on each end of the airfoil to prevent the airfoil from rubbing the test section window/side wall. The chord length was 5.94 in., representing a maximum thickness-to-chord ratio of 7.6 percent. The airfoils had knife leading and trailing edges. Although both leading and trailing edges had a nominal design half-angle of 8.7° for both the convex and wedge surfaces, the lower airfoil (airfoil A) and the upper airfoil (airfoil B) had inspected convex leading-edge half-angles of 8.7° and 8.9° , respectively. Seven midspan pressure ports having a diameter of 0.031 in. were provided at x/c locations of 0.12, 0.25, 0.375, 0.5, 0.628, 0.75, and 0.89. The pressure ports corresponding to these x/c locations were designated as ports A1 to A7 (leading edge to trailing edge) and ports B1 to B7 (leading edge to trailing edge) for airfoils A and B, respectively.

Figure 12 shows that the airfoil is not symmetric about the chord line and that only one of the surfaces is convex. This asymmetry is possible because each cascade passage is aerodynamically isolated from all other passages in a cascade with an SLEL. Thus, these two monoconvex airfoils can simulate an infinite cascade of biconvex airfoils with an SLEL.

3.3 Oscillation Mechanism

The airfoil oscillation mechanism design (fig. 13) was inspired by the NASA Glenn Duct Laboratory's 4- by 10-in. wind tunnel (ref. 23). The oscillation system consists of a barrel cam, a cam follower arm, and a cam follower button. Oscillatory motion about midchord was imparted to airfoil A by the rotating barrel cam (figs. 8 and 14) driven by a 5-hp electric motor (fig. 15). A circular cam follower button attached to the cam follower arm 3 in. away from the airfoil axis of rotation traveled in the three-cycle sinusoidal barrel cam groove. As the barrel cam rotated, the sinusoidal cam groove transmitted an oscillatory motion to the cam follower button, which in turn provided an oscillatory motion to the cam follower arm and thus to the airfoil. The cam follower arm and button were connected to the airfoil boss as shown in figure 16. The barrel cam was mounted on a shaft by using a split taper bushing. The mean

angle of attack about which airfoil A oscillated could be adjusted by the longitudinal position of the barrel cam on the shaft as indicated in figure 13(b).

The cam and cam button were made of 440C stainless steel. The cam was heat treated to Rockwell 62 hardness. The button was heat treated to Rockwell 55 hardness to ensure that the button would wear before the cam. The cam, follower arm, and button were mounted inside a Plexiglas lubrication enclosure (see fig. 8). Lubrication was provided by completely immersing the cam, follower arm, and button in 85W-140 gear oil.

4.0 Instrumentation

The instrumentation used in the experimental facility falls into two groups. The first group, called steady-state data instrumentation, was used for acquiring the various wind tunnel calibration data, including the steady-state airfoil pressures and the wind tunnel operating conditions, for each wind tunnel run. The second group, called unsteady data instrumentation, was used to measure the unsteady pressures on the oscillating cascade. The following sections describe the steady and unsteady instrumentation.

4.1 Steady-State Data Instrumentation

A thermocouple located upstream of the last screen of the settling chamber was used to measure stagnation temperature (see fig. 4). A total pressure probe located downstream of the last screen in the convergent portion of the wind tunnel was used to measure stagnation or total pressure. The total pressure probe was connected in parallel to the Scanivalve pressure-measuring system and to a separate total pressure transducer. Static pressure was measured on the floor of the test section by using a static pressure port. The static port was located upstream of any possible oblique shock waves emanating from the airfoils. The static port was likewise connected in parallel to both the Scanivalve pressure transducer and a separate static pressure transducer. The separate transducers were used to monitor the tunnel total and static pressures throughout the wind tunnel run.

The Scanivalve system consisted of two sample-and-hold modules connected to one Scanivalve pressure transducer with a range of 0 to 100 psig and a sensitivity of 0.2 mV/psi. The separate total and static pressure transducers had a range of 0 to 100 psig and a sensitivity of 0.01 V/psi.

Bay signal conditioning units provided excitation voltage, bridge balancing, and amplification for the Scanivalve, the wind tunnel steady-state pressure transducers, and the thermocouple. The steady-state signals (except for the steady-state signals from the Kulite pressure transducers mounted in the airfoil) were passed through a low-pass filter set at 10 Hz. The steady-state pressure signals were converted to digital signals by using a ± 1 -V Datel model 256 analog-to-digital (A/D) convertor with 14-bit resolution.

4.2 Unsteady Data Instrumentation

Kulite model XCS-093-25-A pressure transducers having a range of 0 to 25 psia were installed in the airfoils. The transducers had a nominal sensitivity of 10 mV/psi at 5-Vdc excitation. Each transducer (with an outside diameter of 0.095 in.) was mounted in a stainless steel sleeve with an inside diameter of 0.1 in. and an outside diameter of 0.13 in. The sleeve and transducer assemblies were in turn mounted in the 0.138-in.-diameter airfoil instrumentation orifices as shown in figure 17. Dow Corning 3140 room-temperature-vulcanizing (RTV) silicone coating was used to mount the transducer in the sleeve and the sleeve/transducer assembly in the airfoil instrumentation orifices. The sleeve provided a means for installing and removing the pressure transducers without damaging them. The sleeve could be gripped

with pliers, or a small wire could be inserted into a hole in the sleeve side wall to pull it out of the airfoil (design concepts from private communication with David Seidel of NASA Langley, February 1991).

The transducers were mounted parallel to the airfoil span such that their pressure-sensing diaphragms lay in the plane of oscillation (chordwise direction), perpendicular to the airfoil axis of rotation. In this manner any apparent pressure response due to motion induced into the pressure diaphragms from the airfoil oscillation was minimized.

The phase angle of the unsteady pressures with respect to the airfoil oscillatory motion were determined by using an Endevco model 7264–2000 accelerometer mounted on the follower arm. The accelerometer was encased in RTV to protect the sensor from the lubricating oil. At 10-Vdc excitation, the nominal output sensitivity was 0.2 mV/g. The accelerometer generated a sinusoidal signal as the airfoil oscillated. The phase angle was computed as the difference between the phase of the unsteady pressures and the phase of the airfoil motion.

The excitation and bridge-balancing units used for the Kulite pressure transducers and the Endevco accelerometer had been manufactured by North American Aviation many years previously. Bay 5303 signal-conditioning units were used to amplify and filter the analog signals. The excitation bridge-balancing and signal-conditioning units were all contained in a portable two-rack system as shown in figure 18. The analog signals were then converted to digital signals by using a Preston ± 10 -V A/D convertor with 15-bit resolution.

Although the Kulites were absolute pressure transducers, they were used as differential transducers. Before each wind tunnel run the transducer bridges were balanced. The output voltage from the transducer (steady state) corresponded to the ambient atmospheric pressure. The unsteady pressures obtained were an offset from the atmospheric. Any damage to a transducer diaphragm would be apparent by inspecting the output voltage (steady state), with the correct voltage corresponding to atmospheric pressure.

A crucial aspect of this type of experiment is to maintain a constant airfoil oscillation frequency. When obtaining unsteady pressures on a cascade with stagger by using the influence coefficient technique, two separate wind tunnel runs are required in which the airfoil oscillation frequencies need to be constant and the frequencies between the two runs must match. The airfoil oscillation frequency was monitored at the airfoil drive mechanism by using a 12-V digital tachometer connected to a magnetic probe. The magnetic probe was placed in close proximity to the drive pulley split taper bushing. The bushing contained a slot that provided a once-per-revolution signal as it passed by the probe. Airfoil oscillation frequency was determined from knowing the diameter ratio of the drive pulley to the cam pulley and taking into account that there were three airfoil oscillations to one revolution of the cam. This tachometer setup was used for determining airfoil oscillating frequencies and for matching the oscillating frequencies between wind tunnel runs for cascades with stagger. The airfoil frequencies used for calculating reduced frequencies were determined by performing a discrete Fourier transform (DFT) on the accelerometer signal.

For unsteady testing the oscillation system was started before the wind tunnel. When steady-state airfoil oscillation had been achieved, the wind tunnel was started. Unsteady data were collected when the tunnel conditions indicated supersonic flow.

5.0 Data Acquisition

Steady-state pressures were acquired by using both the Scanivalve system and the Kulite pressure transducers. With the wind tunnel test section at Mach 1.9 the Scanivalve sample-and-hold modules were activated, trapping the pressures in the modules, where they were subsequently sampled in sequence by using the Scanivalve pressure transducer. All wind tunnel calibration data and the first series of steady-state cascade pressures were acquired in this manner.

As previously stated, the Kulites were also used to measure the steady pressures on the airfoils. The acquisition technique for steady pressure data using the Kulites was the same as for the acquisition of unsteady data described in the following text.

The magnitude and phase of the unsteady pressures were acquired by using Kulite pressure transducers and an Endevco accelerometer as previously mentioned. Fifteen Preston sample-and-hold cards were used for simultaneous sampling of the 14 Kulite pressure transducer signals and the Endevco accelerometer signal. With the tunnel operating at Mach 1.9 and airfoil A oscillating at a near constant frequency, the electronic sample-and-hold cards were activated while retaining the various voltages output from the transducers until they were processed by the Preston A/D convertor. The data sample-and-hold process was accomplished at a rate of 10 kHz. After the unsteady pressure data were acquired, the wind tunnel total temperature and total and static pressures were recorded by using the Scanivalve system. The tunnel was then shut down.

A wideband filter was used to attenuate signals above 25 kHz. Figure 19 shows a typical calibration curve from one of the amplifiers. The amplifiers provided a flat gain response from direct current to 20 kHz, with a 3-dB rolloff at 25 kHz. According to the Nyquist frequency criteria, signals between 5 kHz and 25 kHz would be “wrapped” around the DFT window. If any frequencies of these alias signals were an integer multiple of the unsteady pressure signals, erroneous pressure magnitudes would result. Upon inspection of a typical power spectrum of the unsteady pressure signals as shown in figure 20, one can intuitively see that there was insignificant signal content above the first harmonic. This result was typical. Thus, although aliasing did occur, it was not believed to be an overriding problem in our case.

6.0 Wind Tunnel Calibration

The flow characteristics of the wind tunnel were determined so that the unsteady aerodynamic data could be properly reduced. Mainly, wind tunnel calibration consisted of determining the test section Mach number and flow angle. These two quantities were determined prior to unsteady airfoil testing.

6.1 Mach Number

The test section Mach number was measured by operating the tunnel empty and measuring the static pressure on the roof and floor of the test section. Figure 21 is a plot of p/p_0 for the floor and roof versus distance along the tunnel axis (starting after the throat and continuing through the test section). The test section p/p_0 pressure ratio corresponded to that for Mach 1.97 flow. Thus, supersonic flow in the test section was confirmed.

6.2 Flow Angle

The next series of tests consisted of measuring the flow angle in the test section. A flow angle wedge (fig. 22) was installed in the airfoil A position in the tunnel test section. The flow angle wedge had one static pressure orifice at midspan on each side of its 18° (half-angle) wedge. The wedge was positioned at -1°, 0°, and 1° angles of attack. Comparing the upper and lower surface pressures determined that the flow was essentially parallel to the tunnel centerline at the test section.

The presence of the airfoils in the wind tunnel would change the flow in the test section and could also introduce enough flow blockage to result in a subsonic leading-edge locus on the cascade. Thus, the flow field in the test section with the airfoils installed was investigated, in several steps, to check for any undesirable characteristics. First, the wind tunnel was operated with only airfoil A installed. Pressures on

the convex surface of the airfoil were measured at 1° , 0° , and -1° angles of attack. Figures 23(a) and (b) compare the experimental pressures obtained by using the Scanivalve system with pressures predicted by shock expansion theory for an airfoil at 0° and $\pm 1^\circ$ angles of attack, respectively. Experimental data at x/c of 0.625 were not included because an obstruction in the pressure tubing prevented proper pressure measurement. Experiment and theory correlated well.

The wind tunnel was operated with both airfoils A and B installed. Steady-state pressures were measured on the convex surfaces of both airfoils at stagger angles of 0° , 10° , and 20° . Figure 24 compares experimental pressures (obtained by using the Scanivalve system) with Euler CFD code predictions (ref. 18) for a stagger angle of 0° . The correlation was very good. Figures 25 and 26 compare experimental pressures obtained by using the Scanivalve system and the Kulite pressure transducers with CFD prediction for stagger angles of 10° and 20° , respectively. The Kulites did not correlate as well with the theory at the trailing edge as did the pressures measured by the Scanivalve system.

Looking at the correlation of theory with the Scanivalve data, it can be concluded that the cascade did indeed have a supersonic leading-edge locus. It can also be concluded that the free-stream Mach number was 1.97 and the flow behaved well.

7.0 Unsteady Data Reduction

This section describes the methods by which the unsteady experimental data were transformed into influence coefficients. The unsteady, analog, time-history voltage output from the transducers was converted into discrete time-history pressure and acceleration values by using an A/D convertor and the transducer sensitivities. Because the DFT was required to calculate the influence coefficients and the DFT routine (ref. 24) required 2^n data points, the number of discrete data samples was limited to quantities of 2^n , where $1 < n < 15$. For each transducer 32 768 ($n = 15$) data samples were acquired simultaneously, at a rate of 10 000 samples/sec, resulting in a data acquisition time of 3.2768 sec for each wind tunnel run. Consequently, the time increment between samples was 0.0001 sec.

As previously stated, the 15 transducer time histories consisted of 32 768 data points each. The time histories were then divided into blocks of data with 2^n samples each, where n was either 11, 12, or 13, resulting in 2048, 4096, or 8192 points, respectively. The optimum choice of the order n was determined by calculating the unsteady pressure coefficients for all three values of n and then choosing the data with the smallest uncertainty based on a ± 95 percent confidence interval obtained by using a “t” statistical distribution.

One characteristic of a blowdown wind tunnel is that the total pressure and hence the static pressure in the test section decrease with time. Thus, the sinusoidal pressure-time history contained a nonoscillatory decreasing static pressure component. The data were consequently detrended to remove the nonoscillatory component such that the sinusoidal pressure-time history contained only unsteady pressure components.

FORTTRAN software was used to transform the 15 transducer time histories into 14 unsteady pressure magnitude and phase values. The code was provided by Dr. Dan Buffum of NASA Glenn and was modified for use at The Ohio State University. The flowchart in figure 27 presents, in a general and condensed manner, the process of transforming the transducer time histories into magnitude and phase. This process will be described next.

Referring to figure 27, the accelerometer time history consisting of 32 768 data points was divided into 16 blocks of data (assuming $n = 11$) containing 2048 data points each. A Hanning window was applied to each block. The phase angle of the first harmonic of the airfoil oscillation signal for each block was determined by using a DFT routine and interpolating (ref. 25) to correct for leakage (see appendix B). The acceleration harmonics were converted into displacement harmonics before

interpolation. Thus, 16 phase angles of the airfoil oscillation, corresponding to the 16 data blocks, were determined.

Next, the time history of the unsteady pressure for port A1 (the transducer nearest the leading edge of airfoil A) was divided into 16 data blocks containing 2048 data points each. A Hanning window was applied to each block. The magnitude and phase angle of the first harmonic of the unsteady pressure were determined by using a DFT and interpolating. However, of interest was the phase angle of the unsteady pressure with respect to airfoil oscillation, and not the phase angle of the unsteady pressure-time history itself. Therefore, the phase angle of interest was determined by subtracting the phase angle of the airfoil oscillation time history from the phase angle of the unsteady pressure-time history, for all 16 data blocks for port A1.

An average magnitude and phase angle of the unsteady pressure-time history were determined by using all 16 data blocks. The magnitude and phase angle resulting from each data block were then compared against the average. Blocks of data with their magnitudes outside ± 20 percent of the average were discarded. Blocks of data with their phase angles in a quadrant opposite the average were also discarded. A new average magnitude and phase angle were computed by using the remaining data blocks. This process was then repeated for the remaining pressure transducers on airfoils A and B.

Thus, the magnitudes and phase angles (with respect to airfoil oscillation) of the first harmonic of the unsteady pressure for 14 transducers were acquired. From the magnitudes and phase angles the real and imaginary components were computed. Each unsteady pressure having a magnitude and phase angle is represented as the complex quantity P_1 in equation (1).

The influence coefficients were calculated by dividing the real and imaginary components of P_1 by $q_\infty \alpha_1$, where q_∞ is given as

$$q_\infty = \gamma p_\infty M_\infty^2 \quad (23)$$

where γ is the ratio of specific heats ($\gamma = 1.4$), p_∞ is the free-stream static pressure, and M_∞ is the free-stream Mach number.

7.1 Free-Stream Mach Number

Assuming isentropic flow, the Mach number was determined by using the measured total pressure in the stagnation chamber and the measured static pressure on the test section floor. Although the total pressure and hence the static pressure decreased during each wind tunnel run, this decreased pressure did not affect the Mach number because it was fixed by the tunnel geometry (ratio of throat to test section area), given that the ratio of static to total pressure was sufficient to maintain supersonic flow.

7.2 Free-Stream Static Pressure

Because the free-stream static pressure p_∞ decreased during a wind tunnel run, an average value was used in equation (23) to calculate the influence coefficients. The static pressure port used to determine Mach number was sampled only at the end of each wind tunnel run. Thus, using this port to provide the static pressure would have resulted in a lower than average static pressure in equation (23) and hence higher than average influence coefficients, which would not be desirable.

Because airfoil B did not oscillate and port B1 was upstream of any shock reflections, the free-stream static pressure was determined by using shock expansion theory and the measured pressure from port B1. Figure 28 presents a flowchart describing this method. From the free-stream Mach number, the airfoil

surface slope at port B1, and the time history of the pressure p_B from port B1, a time history of the free-stream static pressure was obtained. An average p_∞ was determined from the detrended data and used to calculate q_∞ .

7.3 Amplitude of Oscillation

The amplitude of oscillation was measured statically before and/or after the wind tunnel run by using a gunners sight (fig. 29). By clamping a steel plate to the top horizontal flat surface on the north airfoil boss and resting the gunners sight on the plate, the angle of the plate (and hence the airfoil chord line) with respect to level was measured. The angle was measured at the extreme pitch-up and pitch-down positions of the airfoil by contacting the cam follower button on the appropriate inside wall of the barrel cam groove. This measurement was made for all lobes of the barrel cam. Even though the gunners sight had an accuracy to within $\pm 0.0056^\circ$, the measurement of the airfoil oscillation amplitude was not as accurate, in part because of minute deviations in the flatness of the plate. The method of clamping the plate to the airfoil also introduced errors. The wear of the cam follower button introduced play between it and the cam groove, which also made it difficult to measure the exact value of the oscillation amplitude. Despite uncertainties in the exact oscillation amplitude, an amplitude of 1.2° was about midway between the estimated error limits and therefore was used for data reduction. The pitch-up and pitch-down amplitudes were set as nearly equal as possible prior to the wind tunnel runs such that the airfoil oscillated approximately about 0° angle of attack.

8.0 Unsteady Aerodynamic Results

This section compares experimental unsteady pressures with those predicted by three unsteady aerodynamic algorithms for a cascade of airfoils with an SLEL oscillating in pitch about midchord. These algorithms were based on potential theory, piston/potential theory, and the Euler equations.

Reference 9 presents a potential theory solution for the unsteady pressure on a cascade of oscillating airfoils with an SLEL. This approach idealizes the airfoils as flat plates. The streamwise location of shock wave/airfoil impingement is determined by using Mach angles. Nonlinear effects on unsteady pressure and shock wave/airfoil impingement location, due to the airfoil geometry, are not accounted for. Reference 8 presents an algorithm based on this theory, denoted herein as the Lane code.

In an effort to maintain computational efficiency and include some effects of airfoil geometry, a hybrid algorithm was developed to include the nonlinear effects of thickness and camber in the isolated noninterference regions of the airfoils. These regions consisted of the portion of each airfoil upstream of the first shock wave/airfoil impingement location. Because of the SLEL each airfoil surface in this region was aerodynamically isolated from its neighbors. Piston theory was used in this region to account for the nonlinear effects of thickness and camber. Downstream of the first shock wave/airfoil impingement location the potential theory of reference 9 was used. Even though airfoil geometry was accounted for in the isolated noninterference regions of the airfoils, the shock wave/airfoil impingement locations were determined by assuming flat-plate airfoils in conjunction with the use of Mach angles. Reference 12 presents the algorithm and theoretical development for this hybrid approach, denoted herein as the piston code.

Reference 18 describes the computational fluid dynamic algorithm used to solve the Euler equations and provide unsteady pressures for comparison with experiment. This algorithm, referred to herein as the Euler code, solves the two-dimensional unsteady Euler equations by using a time-marching, flux-difference splitting scheme of reference 17 with blocked grids. The Euler code solves the flow equations for one or more H grids, which are allowed to deform with airfoil motion as in reference 16. The

algorithm is third-order accurate in space and second-order accurate in time. The Euler code accounts for the airfoil geometry while solving the inviscid flow equations.

Because comparing experimental and predicted unsteady pressure coefficients for a variety of interblade phase angles would be a time-consuming task, the comparisons presented in this report are for interblade phase angles of 0° and 180° only. However, the reader may generate experimental unsteady pressure difference coefficients for any interblade phase angle by using the unsteady pressure influence coefficients presented in table I and assigning an interblade phase angle value to β in equation (15).

Influence coefficient data covering interblade phase angles of 0° and 180° are presented for 0° and 10° of stagger. The unsteady data (data set) are identified by the corresponding wind tunnel run numbers. Table II presents the wind tunnel operating conditions for the data sets.

8.1 0° Stagger

Figure 30 compares the experimental values of the real and imaginary components and the magnitude and phase angle of ΔC_p for data set 68 with the values predicted by the Lane and piston codes. Figures 31 and 32 present these comparisons and comparisons with the Euler code predictions for data sets 69 and 77, respectively. Data sets 68, 69, and 77 correspond to reduced frequencies of 0.0562, 0.0929, and 0.1457, respectively. Because of undetermined computational difficulties, the Euler code did not run at the low reduced frequency of 0.0562; thus, no comparison was made between its predictions and data set 68.

Figures 30 to 32 show that the various components of the experimental values of ΔC_p change abruptly near $x/c = 0.5$. This abrupt change resulted from the bow shock waves impinging on the downstream airfoil surfaces. The spacing of the seven pressure transducers made it impossible to determine the precise location of the shock wave reflection. For future reference the shock wave/airfoil impingement location from experiment is denoted as x_{s_e} .

8.1.1 Real and imaginary parts of ΔC_p .—The $\text{Re}(\Delta C_p)$ changes from a positive quantity upstream of x_{s_e} to a negative quantity downstream (figs. 30(a), 31(a), and 32(a)), but the $\text{Im}(\Delta C_p)$ behaves in the opposite manner (figs. 30(b), 31(b), and 32(b)). Examining the $\text{Re}(\Delta C_p)$ and $\text{Im}(\Delta C_p)$ in these figures shows that the correlation between experiment and the various algorithms is not as favorable for $\text{Im}(\Delta C_p)$ as for $\text{Re}(\Delta C_p)$. The shock wave/airfoil impingement location predicted by the Lane and piston codes for $\text{Im}(\Delta C_p)$ is about 20 percent downstream of its actual location. For future reference, x_{s_a} denotes the analytically predicted streamwise location of bow shock wave/airfoil impingement based on the Lane and piston codes.

As shown in figures 31(a) and (b) and 32(a) and (b), the Lane code does not correlate with experiment as well as the Euler code for $\text{Re}(\Delta C_p)$ and $\text{Im}(\Delta C_p)$ upstream of x_{s_e} . This result is probably due to airfoil surface curvature, which the Lane code does not account for. The piston code does a better job than the Lane code in this respect. The Euler code correlates better with experiment than either the Lane or piston codes downstream.

8.1.2 Magnitude of ΔC_p .—Figures 30(c), 31(c), and 32(c) compare experimental and predicted values of the magnitude of ΔC_p , denoted as $|\Delta C_p|$ for data sets 68, 69, and 77, respectively. As shown in figures 31(c) and 32(c), the Euler code correlated better than the Lane and piston codes. The Euler code exhibited the same trends as the experiment, with the largest discrepancies occurring around midchord.

8.1.3 Phase angle of ΔC_p .—Figures 30(d), 31(d), and 32(d) compare experimental and predicted phase angles for data sets 68, 69, and 77, respectively. The Euler, Lane, and piston codes all correlated to the same degree with experiment upstream of x_{s_e} . Again, the Lane and piston codes predicted x_s to be

20 percent farther downstream than experiment showed. The Lane and piston codes predicted the shock wave/airfoil impingement location to be farther downstream owing to their inherent assumptions as discussed previously. Downstream of x_{s_a} , the Lane and piston codes predicted phase angles that correlated reasonably well with the experimental values downstream of x_{s_e} . The predicted phase angles from the Euler code correlated well with experiment downstream of x_{s_e} .

After inspection of the unsteady data for 0° stagger it was evident that the experimental and predicted values of the imaginary part of ΔC_p did not correlate as well as the real part in the isolated airfoil regions. The source of this discrepancy is believed to be in part the difference between the experimental and analytical phase angles. As shown in figures 30(d), 31(d), and 32(d) and schematically in the complex plane in figure 33, the phase angles upstream of x_{s_e} are small. Figure 33 shows that any error in the small phase angle σ will affect the imaginary component to a greater extent than the real component. To further corroborate this idea, the phase angles calculated by using the Euler code were used in conjunction with the experimental unsteady pressure magnitudes of data set 69 to determine the real and imaginary components of the unsteady pressure difference ΔC_p . The real and imaginary components of ΔC_p correlated quite well with the Euler-code-calculated components of ΔC_p in the isolated airfoil regions, as shown in figure 34. This correlation confirms that the measurement of the phase angle was one source of the discrepancy between experimental and analytical unsteady pressures. The correlation was also improved downstream of the shock wave/airfoil impingement location, but not as well as upstream.

Several possible causes of phase angle error were possible, including airfoil twisting during oscillation, acoustic effects of the pressure orifice, excessive wear of the cam follower button, as well as possible accelerometer error. Although a malfunctioning accelerometer could have contributed to phase angle error, it was not investigated. However, the other three possible causes were investigated and are discussed next. Airfoil twisting during oscillation could change the actual phase angle between the accelerometer and the pressure transducers because the accelerometer was located on the airfoil arm and the pressure transducers were located at midspan of the airfoil. The phase angle error due to airfoil twisting during oscillation was determined to be negligible by performing a direct transient response on a finite element model of the airfoil using MSC/NASTRAN. The airfoil was modeled by using solid elements. An enforced sinusoidal (time domain) displacement was applied to the airfoil. Oscillation frequencies of 96.14 and 165.74 Hz were imposed. In both cases the phase lag due to airfoil twist was less than 0.4° . There was essentially no amplitude increase.

The phase angle error due to pressure orifice geometry was investigated by Dr. Stephen Whitmore of NASA Ames/Dryden using a CFD code (ref. 26). The analysis estimated that the orifice geometry introduced a pressure phase lag of about 0.4° and a pressure rise of 0.05 dB. These values were considered negligible.

Some phase angle error was very likely introduced by excessive wear of the cam follower button. As the cam follower button wore, the button would tend to slap inside the barrel cam groove instead of smoothly following the groove contour. Thus, the sinusoidal motion of the button and hence the airfoil, as well as the peak airfoil oscillation amplitude, were adversely affected.

8.1.4 180° interblade phase angle.—The previous results for 0° stagger corresponded to an interblade phase angle of 0° . As mentioned before, the experimental influence coefficients may be used to generate the unsteady pressures for any interblade phase angle. As an example, the influence coefficients presented in table I(a) are substituted into equation (15) with $\beta = \pi$, thereby generating the unsteady pressure difference for an interblade phase angle of 180° . Figures 35 to 37 show the real and imaginary parts of the unsteady pressure difference for runs 68, 69, and 77, with an interblade phase angle of 180° . Comparing these figures for $\beta = 180^\circ$ with figures 30(a) and (b), 31(a) and (b), and 32(a) and (b) for $\beta = 0^\circ$ shows that the unsteady pressure difference upstream of x_{s_e} remained unaffected by

the interblade phase angle β , whereas downstream of x_{s_e} the unsteady pressure difference changed both magnitude and sign. The correlation between experiment and the Lane code is lacking, although the Lane code exhibited the general trends.

8.2 10° Stagger

Figure 38 compares the experimental values for $\text{Re}(\Delta C_p)$ and $\text{Im}(\Delta C_p)$ as well as the magnitude and phase angle of ΔC_p with the values predicted by the Euler, Lane, and piston codes for the cascade at 10° stagger. Data sets 84 and 86 were used to generate the influence coefficients. Data set 84 represents influence coefficients $\bar{C}_{p_u}^0$ and $\bar{C}_{p_l}^{-1}$ for a stagger angle of 10°. Data set 86 represents influence coefficients $\bar{C}_{p_l}^0$ and $\bar{C}_{p_u}^1$ for a stagger angle of -10°. Together these two data sets were used to produce the graphs shown in figure 38.

Table II presents the various tunnel flow data for runs 84 and 86. The difference in reduced frequency between data sets 84 and 86 was less than 5.6 percent. The average free-stream static pressures and Mach numbers were within 1 percent and 0.56 percent of each other, respectively.

8.2.1 Real and imaginary parts of ΔC_p .—As shown in figure 38(a) the Euler code correlated better with the $\text{Re}(\Delta C_p)$ than either the Lane or piston codes. Again, the Lane and piston codes placed the shock wave/airfoil impingement locations farther downstream than did the experiment for the aforementioned reasons. Figure 38(b) shows that the experimental values of the $\text{Im}(\Delta C_p)$ did not correlate well with any of the codes. The $\text{Im}(\Delta C_p)$ as predicted by the Lane and piston codes would correlate better between x/c values of 0.4 and 0.78 if the analytical shock wave/airfoil impingement locations were shifted upstream by 20 percent.

8.2.2 Magnitude of ΔC_p .—Figure 38(c) compares the experimental and calculated values of $|\Delta C_p|$. Again, the inherent assumptions of the Lane and piston theories placed the analytical pressure jumps due to shock wave/airfoil impingement approximately 20 percent farther downstream than did the experiment.

8.2.3 Phase angle of ΔC_p .—As shown in figure 38(d) the phase angle as predicted by the Euler code correlated better with experiment than did the Lane or piston codes. The Lane, piston, and Euler codes were in close agreement upstream of 0.4 x/c .

8.2.4 180° interblade phase angle.—The previous results for the 10° stagger cascade corresponded to an interblade phase angle of 0°. The unsteady pressure difference for an interblade phase angle of 180° was generated by substituting the influence coefficients from table I(b) into equation (15) with $\beta = \pi$. Figure 39 shows the real and imaginary parts of the unsteady pressure difference for runs 84 and 86 with an interblade phase angle of 180°. Comparing these figures for $\beta = 180^\circ$ with figures 38(a) and (b) for $\beta = 0^\circ$ shows that the unsteady pressure difference upstream of the first shock wave/airfoil impingement location ($x/c < 0.375$) remained unaffected by the interblade phase angle. Correlation between experiment and the Lane code appeared to be lacking.

9.0 Conclusions

An experimental influence coefficient technique was used to obtain unsteady aerodynamic influence coefficients and unsteady pressures for a cascade of airfoils oscillating in pitch about midchord. Stagger angles of 0° and 10° were investigated for a cascade with a gap-to-chord ratio of 0.417 operating at an

axial Mach number of 1.9, resulting in a supersonic leading-edge locus. Reduced frequencies ranged from 0.056 to 0.2. Influence coefficients were obtained from which the unsteady pressures for any interblade phase angle could be determined. The unsteady pressures were compared with those predicted by several algorithms for interblade phase angles of 0° and 180°.

This experimental program has laid the foundation for future unsteady aerodynamic cascade testing in the supersonic leading-edge-locus flow regime. The correlation of experimental and analytical results was sufficient to conclude that the two-airfoil technique is a good approach for simulating an oscillating cascade of symmetric airfoils with a supersonic leading-edge locus and obtaining experimental influence coefficients. It is hoped that this effort will be of value to future experimental unsteady aerodynamic testing endeavors.

The following conclusions pertain to this specific experimental effort:

1. Piston theory does reflect the general effects of airfoil geometry on unsteady pressure in the isolated airfoil regions of this cascade.
2. The Lane, piston, and Euler codes all predict similar phase angles between the airfoil motion and the unsteady pressure. Thus, it is evident that the airfoil thickness distribution does not have a large effect on the unsteady-pressure phase angle.
3. In general, the Euler code correlates better with experiment than do either the Lane or piston codes for the airfoils considered in this study.
4. One major finding of this work is that the Lane and piston codes do not accurately locate the shock wave/airfoil impingement locations partly because of flat-plate airfoil assumptions. Even though the piston code accounts for airfoil geometry in the isolated airfoil regions, the shock wave/airfoil impingement locations are still based on flat-plate geometry. The unsteady pressures predicted by the Lane and piston codes could be greatly improved by repositioning the shock wave/airfoil impingement locations by using a steady-flow theory (e.g., the method of characteristics or a steady CFD flow solver) that accounts for airfoil geometry.
5. Phase angle errors can be greatly reduced in future endeavors by improving the airfoil/oscillating mechanism. These improvements can be incorporated with little difficulty. In particular, the airfoils could be made from a lighter material, such as titanium, along with smaller trunnions, reducing the airfoil/oscillating mechanism inertia characteristics and thereby reducing cam follower button wear. The cam follower button diameter could also be made larger to provide better wear performance. Minimizing cam follower button wear would provide more accurate sinusoidal airfoil oscillations, resulting in more accurate phase angles of the unsteady aerodynamic influence coefficients and thus providing more accurate unsteady pressures.

Appendix A Symbols

A	calculated estimate of amplitude
A_g	given amplitude of cosine wave
A_h	maximum amplitude of the weighting function for Hanning window
A_r	maximum amplitude of the weighting function for rectangular window
b	half chord, $c/2$
C_{pl}	pressure coefficient for lower surface of reference airfoil ($n = 0$) as defined in eq. (2)
C_{pu}	pressure coefficient for upper surface of reference airfoil ($n = 0$) as defined in eq. (2)
\bar{C}_{pl}^0	influence coefficient for unsteady pressure on lower surface of reference airfoil ($n = 0$) due to oscillation of reference airfoil (see fig. 1)
\bar{C}_{pl}^1	influence coefficient for unsteady pressure on lower surface of reference airfoil ($n = 0$) due to oscillation of airfoil $n = 1$ (see fig. 1)
\bar{C}_{pl}^{-1}	influence coefficient for unsteady pressure on lower surface of reference airfoil ($n = 0$) due to oscillation of airfoil $n = -1$ (see fig. 1)
\bar{C}_{pu}^0	influence coefficient for unsteady pressure on upper surface of reference airfoil ($n = 0$) due to oscillation of reference airfoil (see fig. 1)
\bar{C}_{pu}^1	influence coefficient for unsteady pressure on upper surface of reference airfoil ($n = 0$) due to oscillation of airfoil $n = 1$ (see fig. 1)
\bar{C}_{pu}^{-1}	influence coefficient for unsteady pressure on upper surface of reference airfoil ($n = 0$) due to oscillation of airfoil $n = -1$ (see fig. 1)
ΔC_p	pressure difference coefficient as defined in eq. (14)
c	airfoil chord
c_l	two-dimensional lift coefficient as defined in eq. (12)
c_m	two-dimensional moment coefficient as defined in eq. (13)
F_s	sampling frequency
f	calculated estimate of frequency
f_g	given frequency of cosine wave
$f_{u,u+1}$	frequency component from discrete Fourier transform corresponding to bin u or $u + 1$
g	gravitational constant
$\text{Im}(\dots)$	imaginary part of (\dots)
k	reduced frequency, $\omega b/V$
l	subscript or superscript denoting lower surface of reference airfoil ($n = 0$)
$M_{u,u+1}$	amplitude of frequency component from discrete Fourier transform corresponding to bin u or $u + 1$
M_∞	free-stream Mach number
N	(number of airfoils $- 1$)/2; number of data samples

n	airfoil index; also order of discrete Fourier transform
P_1	complex-valued first harmonic of unsteady pressure signal
P, P_{s_1}	static pressure
P_B	static pressure at airfoil port B1
p_∞	free-stream static pressure
P_0, P_{t_i}	stagnation or total pressure, $i = 1, 2$
q_∞	free-stream dynamic pressure
R	ratio of two largest magnitudes of frequency spectrum
$\text{Re}(\dots)$	real part of (...)
s	blade spacing as shown in fig. 1
t	time
u	subscript or superscript denoting upper surface of reference airfoil ($n = 0$); discrete Fourier transform bin index
V	free-stream velocity
x	streamwise coordinate
x_M	streamwise location of shock wave/airfoil impingement from neighboring airfoil, as predicted by algorithms
x_s^l	shock wave/airfoil impingement location on lower surface of reference airfoil
x_s^u	shock wave/airfoil impingement location on upper surface of reference airfoil
x_{s_a}	shock wave/airfoil impingement location from analysis
x_{s_e}	shock wave/airfoil impingement location from experiment
y	transverse coordinate
α_1	amplitude of reference airfoil oscillation
β	interblade phase angle; frequency change between consecutive bins
γ	ratio of specific heats (1.4 in this work)
δ	surface slope
θ	stagger angle; calculated estimate of phase angle; oblique shock wave angle
θ_g	given phase angle of cosine wave
$\theta_{u,u+1}$	phase angle of frequency component from discrete Fourier transform corresponding to bin u or $u + 1$
ν	ratio defined in eq. (B2)
σ	phase angle
σ_a	phase angle of airfoil acceleration-time history
σ_d	phase angle of airfoil oscillation (displacement)-time history
σ_p	phase angle of unsteady pressure-time history
φ_p	phase angle of unsteady pressure with respect to airfoil oscillation
ω	circular frequency

Appendix B Leakage Correction

This appendix describes the phenomenon of leakage by example, which it is hoped will give the reader a basic understanding of leakage and how it is corrected for in data reduction procedures. The equations used for leakage correction in this appendix were obtained from the notes of Dr. Don Braun of NASA Glenn. Appendix A of reference 21 and reference 25 discuss the derivation of these equations, although different variables are used.

Consider a continuous cosine wave having an amplitude of $A_g = 1$, a frequency of $f_g = 1000$ Hz, and a phase angle of $\theta_g = 0^\circ$. Suppose this wave is sampled at a rate of $F_s = 4000$ samples/sec, capturing $N = 4096$ discrete data samples. Furthermore, suppose a rectangular window (each data point multiplied by a factor of $A_r = 1$) is applied to the sampled data starting at $t = 0$. The end of the rectangular window would be at $N/F_s = 1.024$ sec, corresponding to the total time for data acquisition. Exactly $f_g N/F_s = 1024$ cycles of the cosine wave would be within the rectangular window, represented by the 4096 discrete data samples.

Performing a discrete Fourier transform on the 4096 data samples within the rectangular window would result in the frequency spectrum shown in figure 40(a). There all components in the frequency domain have an amplitude of 0 except for the frequency components at ± 1000 Hz. The amplitudes of the frequency components at ± 1000 Hz are both 0.5, each corresponding to one-half of the amplitude of the continuous cosine wave.

It is sufficient to look only at the positive frequency spectrum and multiply the amplitude of the frequency component at 1000 Hz by 2 to get the correct amplitude of the cosine wave. This result is possible only because there was an integer number of cosine wave cycles in the rectangular window. Consequently, a frequency component at 1000 Hz in the frequency spectrum corresponded to the exact oscillation frequency (1000 Hz) of the cosine wave. Thus, multiplying the amplitude of the 1000-Hz component by 2 produced the correct amplitude. Moreover, inspecting the actual real and imaginary components of the amplitude of the 1000-Hz frequency component would show that the phase angle is 0° . However, rarely is there an integer number of cycles of a signal in a data window. When the data window does not contain an integer number of cycles of a signal, "leakage" will result.

Consider a continuous cosine wave having an amplitude of $A_g = 1$, a frequency of $f_g = 1000$ Hz, and a phase angle of $\theta_g = 0^\circ$, just as before. However, suppose this wave is sampled at $F_s = 3900$ samples/sec, capturing $N = 4096$ discrete data samples. Furthermore, suppose a rectangular window is also applied to the sampled data starting at $t = 0$ sec. The end of the window would be at $N/F_s = 1.050256$ sec (to seven significant digits), corresponding to the total time for data acquisition. There would be approximately $f_g N/F_s = 1050.256$ cycles of the continuous cosine wave within the window, represented by the 4096 discrete data samples.

Performing a discrete Fourier transform on the 4096 data samples within the rectangular window would result in the positive frequency spectrum shown in figure 40(b) where each DFT frequency bin has a width of $\beta = F_s/N = 0.9521484$ Hz. A closer look at the positive frequency spectrum (fig. 40(c)) reveals no frequency component at the cosine wave frequency of 1000 Hz. The same situation occurs in the negative frequency spectrum, both the result of not having an integer number of cosine wave cycles in the data window. The frequency components containing the largest amplitudes are located in bin number $u = 1050$ at frequency $f_u = u\beta = 999.7559$ Hz and in bin $u + 1 = 1051$ at $f_{u+1} = (u + 1)\beta = 1000.708$ Hz. Taking power from the 1000-Hz frequency component that existed in the continuous cosine wave and distributing this power to frequency components in the frequency spectrum that did not exist in the

continuous wave, such as at 999.7559 Hz and 1000.708 Hz (the predominant components among many others), is known as leakage.

Referring to figure 40(c), the amplitudes for the frequency components at $f_u = 999.7559$ Hz and $f_{u+1} = 1000.708$ Hz are $M_u = 0.4477416$ and $M_{u+1} = 0.1542751$, respectively. The corresponding phase angles are $\theta_u = 46.14598^\circ$ (0.8053993 rad) and $\theta_{u+1} = -133.8233^\circ$ (-2.335657 rad), respectively. It is obvious that the correct frequency, magnitude, and phase angle of the continuous cosine wave do not correspond to any frequency components in the spectrum but lie between the frequency components with the largest amplitudes. The correct amplitude would be as represented by the dashed vertical line at 1000 Hz. To approximate the correct amplitude and phase angle of the original continuous cosine wave, a method of interpolation is used.

As previously stated, a rectangular window was applied to the data. Equations (B1) to (B9) are used to correct for leakage when a rectangular window has been applied to the data. The following discussion presents the interpolation calculations for the 1050.256 cycles of data in the rectangular window. The first step in correcting for leakage is to compute the ratio of the two largest magnitudes of the frequency spectrum, denoted as M_u and M_{u+1} (fig. 40(c)). The ratio yields

$$R = \frac{M_u}{M_{u+1}} = \frac{0.4477416}{0.1542751} = 2.902229 \quad (\text{B1})$$

Next the following ratio is computed:

$$\nu \approx \frac{1}{1 + R} = 0.2562638 \quad (\text{B2})$$

Dividing the sampling frequency by the number of discrete data samples gives the frequency change between consecutive DFT bins as

$$\beta = \frac{F_s}{N} = \frac{3900}{4096} = 0.9521484 \text{ Hz} \quad (\text{B3})$$

Because the frequency component at f_u has a higher energy content than that at f_{u+1} , corresponding to $0 \leq \nu \leq 1/2$, equations (B4) to (B6) are used to estimate the frequency, amplitude, and phase angle, respectively, of the cosine wave. If the frequency component at f_{u+1} had a higher energy content than that at f_u , corresponding to $1/2 \leq \nu \leq 1$, equations (B7) to (B9) would be used instead. The estimate of the frequency is then given as

$$f = f_u + \nu\beta \quad (\text{B4})$$

The estimate of the amplitude is given as

$$A \approx \frac{2N \sin\left(\frac{\pi\nu}{N}\right)}{A_r \sin(\pi\nu)} M_u \approx \frac{2\pi\nu}{A_r \sin(\pi\nu)} M_u \quad (\text{B5})$$

where $\pi\nu$ is in radians. The second part of equation (B5) is valid for large N , where A_r is the weighting function for the rectangular window and is equal to 1 for the DFT program used in this example.

Finally, the estimate of the phase angle is given as

$$\theta \approx \theta_u - \frac{\pi(N-1)v}{N} \quad (\text{B6})$$

where 2π should be added to that value of θ if it is less than $-\pi$ to make the final value of θ in the standard range between $-\pi$ and π . Upon substituting f_u , M_u , and θ_u , which are known from the DFT, and v and β from equations (B2) and (B3) into equations (B4) to (B6), the following estimates of frequency, amplitude, and phase angle for the cosine wave are obtained:

$$\begin{aligned} f &= 999.9999 \text{ Hz} \\ A &= 1.000068 \\ \theta &= 0.0005194 \text{ rad} = 0.02975831^\circ \end{aligned}$$

As is shown, good approximations to the actual frequency, amplitude, and phase angle result.

As previously stated, when $1/2 \leq v \leq 1$ and a rectangular window is applied to the data, the following equations should be used instead of equations (B4) to (B6).

$$f = f_{u+1} - (1-v)\beta \quad (\text{B7})$$

$$A \approx \frac{2N \sin\left[\frac{\pi(1-v)}{N}\right]}{A_r \sin[\pi(1-v)]} M_{u+1} \approx \frac{2\pi(1-v)}{A_r \sin[\pi(1-v)]} M_{u+1} \quad (\text{B8})$$

and

$$\theta \approx \theta_{u+1} + \frac{\pi(N-1)(1-v)}{N} \quad (\text{B9})$$

where 2π should be subtracted from that value of θ if it is greater than π .

Because of its desirable characteristics, a Hanning window was used in the data reduction for this report. Presented here are the equations that should be used to correct for leakage when a Hanning window is applied to the discrete data. Equations (B10) to (B12) should be used to approximate the frequency, amplitude, and phase angle of a waveform when $0 \leq v \leq 1/2$:

$$f = f_u + v\beta \quad (\text{B10})$$

$$A \approx \frac{2N \left\{ 1 - \frac{\left[\tan\left(\frac{\pi v}{N}\right) \right]^2}{\left[\tan\left(\frac{\pi}{N}\right) \right]^2} \right\} \sin\left(\frac{2\pi v}{N}\right)}{A_h \sin(\pi v)} M_u \approx \frac{4\pi(1-v^2)v}{A_h \sin(\pi v)} M_u \quad (\text{B11})$$

and

$$\theta \approx \theta_u - \pi v \quad (\text{B12})$$

where 2π should be added to the value of θ if it is less than $-\pi$.

The following equations should be used to correct for leakage when a Hanning window is applied to the discrete data and $1/2 \leq v \leq 1$:

$$f = f_{u+1} - (1 - v)\beta \quad (\text{B13})$$

$$A \approx \frac{2N \left\{ 1 - \left[\frac{\tan\left(\frac{\pi(1-v)}{N}\right)}{\tan\left(\frac{\pi}{N}\right)} \right]^2 \right\} \sin\left(\frac{2\pi(1-v)}{N}\right)}{A_h \sin[\pi(1-v)]} M_{u+1} \approx \frac{4\pi v(2-v)(1-v)}{A_h \sin(\pi v)} M_{u+1} \quad (\text{B14})$$

and

$$\theta \approx \theta_{u+1} + \pi(1 - v) \quad (\text{B15})$$

where 2π should be subtracted from that value of θ if it is greater than π .

References

1. Franciscus, L.C.: The Supersonic Through-Flow Turbofan for High Mach Propulsion. AIAA Paper 87-2050 (NASA TM-100114), 1987.
2. Ziemanski, J.A., et al.: High Speed Propulsion Technology. Aeropropulsion 1987, NASA CP-10003, 1987.
3. Klapproth, J.F.: A Review of Supersonic Compressor Development. J. Eng. Power, vol. 83, series A, no. 3, 1961, pp. 258-268.
4. Savage, M.; Boxer, E.; and Erwin, J.R.: Resume of Compressor Research at the NACA Langley Laboratory. J. Eng. Power, vol. 83, series A, no. 3, 1961, pp. 269-285.
5. Breugelmans, F.A.E.: The Supersonic Axial Component in a Compressor. ASME Paper 75-GT-26, 1975.
6. Schmidt, J.F., et al.: Supersonic Through-Flow Fan Design. AIAA Paper 87-1746 (NASA TM-88908), 1987.
7. Wood, J.R., et al.: Application of Advanced Computational Codes in the Design of an Experiment for a Supersonic Throughflow Fan Rotor. ASME Paper 87-GT-160, 1987.
8. Ramsey, J.K.; and Kielb, R.E.: A Computer Program for Calculating Unsteady Aerodynamic Coefficients for Cascades in Supersonic Axial Flow. NASA TM-100204, 1987.
9. Lane, F.: Supersonic Flow Past an Oscillating Cascade With Supersonic Leading-Edge Locus. J. Aero. Sci., vol. 24, no. 1, 1957, pp. 65-66.
10. Kielb, R.E.: MISER2—Mistuning Effects on Turbofan Cascades. LEW-14380, COSMIC, University of Georgia, Athens, GA, 1986.
11. Kielb, R.E.; and Ramsey, J.K.: Flutter of a Fan Blade in Supersonic Axial Flow. J. Turbomachinery, vol. III, no. 4, 1989, pp. 462-467.
12. Ramsey, J.K.: Semi-Nonlinear Code for Calculating Unsteady Aerodynamic Coefficients for Cascades in Supersonic Axial Flow. NASA TM-102573, 1991.
13. Ramsey, J.K.: Influence of Thickness and Camber on the Aeroelastic Stability of Supersonic Throughflow Fans. J. Propulsion, vol. 7, no. 3, 1991, pp. 404-411.
14. Huff, D.L.: Numerical Analysis of Supersonic Flow Through Oscillating Cascade Sections by Using a Deforming Grid. AIAA Paper 89-2805 (NASA TM-102053), 1989.
15. Kao, Y.F.: Two-Dimensional Unsteady Analysis for Transonic and Supersonic Cascade Flows. Ph.D. Thesis, Purdue Univ., 1989.
16. Huff, D.L.: Numerical Analysis of Flow Through Oscillating Cascade Sections. AIAA Paper 89-0437 (NASA TM-101417), 1989.
17. Whitfield, D.L.; Janus, J.M.; and Simpson, L.B.: Implicit Finite Volume High Resolution Wave-Split Scheme for Solving the Unsteady Three-Dimensional Euler and Navier-Stokes Equations on Stationary or Dynamic Grids. Mississippi State Engineering and Industrial Research Station Report MSSU-EIRS-ASE-88-2, 1988.
18. Huff, D.L.; Swafford, T.W.; and Reddy, T.S.R.: Euler Flow Predictions for an Oscillating Cascade Using a High Resolution Wave-Split Scheme. NASA TM-104377, 1991.
19. Erwin, D.; Gregorek, G.M.; and Ramsey, J.: Experimental Unsteady Pressures on an Oscillating Cascade With Supersonic Leading Edge Locus. AIAA Paper 92-4035, 1992.
20. Erwin, D.: Design and Initial Testing of a Facility to Measure Unsteady Pressures on an Oscillating Cascade With Supersonic Leading Edge Locus. Ph.D. Thesis, The Ohio State Univ., 1993.
21. Buffum, D.H.; and Fleeter, S.: Aerodynamics of a Linear Oscillating Cascade. NASA TM-103250, 1990.
22. Korn, G.; and Korn T.: Mathematical Handbook for Scientists and Engineers. McGraw-Hill, New York, 1961.
23. Boldman, D.R.; and Buggele, A.E.: Wind Tunnel Tests of a Blade Subjected to Midchord Torsional Oscillation at High Subsonic Stall Flutter Conditions. NASA TM-78998, 1978.
24. Bergland, G.D.; and Dolan, M.T.: Fast Fourier Transform Algorithms. Programs for Digital Signal Processing, IEEE Press, New York, 1979.
25. Burgess, J.C.: On Digital Spectrum Analysis of Periodic Signals. J. Acoust. Soc. Am., vol. 58, no. 3, 1975, pp. 556-567.
26. Whitmore, S.A.; and Mose, T.R.: Effects of Pressure Sensor Acoustics on Air Data Derived From a High Angle-of-Attack Flush Air Data Sensing (HI-FADS) System. NASA TM-101736, 1991.

TABLE I.—UNSTEADY PRESSURE INFLUENCE COEFFICIENTS
(a) Stagger angle $\theta = 0^\circ$

(a1) Upper surface				(a2) Lower surface			
Ratio of streamwise coordinate to airfoil chord, x/c	Run			Ratio of streamwise coordinate to airfoil chord, x/c	Run		
	68	69	77		68	69	77
	Reduced frequency, k				Reduced frequency, k		
	0.0562	0.0929	0.1457		0.0562	0.0929	0.1457
	Influence coefficients for unsteady pressure on upper surface due to oscillation of reference airfoil, $\bar{C}_{p_u}^0$				Influence coefficients for unsteady pressure on lower surface due to oscillation of reference airfoil, $\bar{C}_{p_l}^0$		
0.120	-0.8154 +0.1451 <i>i</i>	-0.8528 +0.1522 <i>i</i>	-0.9122 +0.2491 <i>i</i>	0.120	0.8154 -0.1451 <i>i</i>	0.8528 -0.1522 <i>i</i>	0.9122 -0.2491 <i>i</i>
0.250	-0.7505 +0.1201 <i>i</i>	-0.7650 +0.1174 <i>i</i>	-0.8196 +0.2032 <i>i</i>	0.250	0.7505 -0.1201 <i>i</i>	0.7650 -0.1174 <i>i</i>	0.8196 -0.2032 <i>i</i>
0.374	-0.6887 +0.1181 <i>i</i>	-0.7067 +0.1205 <i>i</i>	-0.7383 +0.2022 <i>i</i>	0.374	0.6887 -0.1181 <i>i</i>	0.7067 -0.1205 <i>i</i>	0.7383 -0.2022 <i>i</i>
0.500	-0.7211 +0.0870 <i>i</i>	-0.7569 +0.06557 <i>i</i>	-0.7577 +0.1126 <i>i</i>	0.500	0.7211 -0.0870 <i>i</i>	0.7569 -0.06557 <i>i</i>	0.7577 -0.1126 <i>i</i>
0.627	-0.7963 +0.1099 <i>i</i>	-0.8350 +0.09825 <i>i</i>	-0.8837 +0.1645 <i>i</i>	0.627	0.7963 -0.1099 <i>i</i>	0.8350 -0.09825 <i>i</i>	0.8837 -0.1645 <i>i</i>
0.750	-0.6437 +0.0919 <i>i</i>	-0.6587 +0.08151 <i>i</i>	-0.6937 +0.1350 <i>i</i>	0.750	0.6437 -0.0919 <i>i</i>	0.6587 -0.08151 <i>i</i>	0.6937 -0.1350 <i>i</i>
0.890	-0.4829 +0.05467 <i>i</i>	-0.4883 +0.03536 <i>i</i>	-0.4893 +0.03686 <i>i</i>	0.890	0.4829 -0.05467 <i>i</i>	0.4883 -0.03536 <i>i</i>	0.4893 -0.03686 <i>i</i>
	Influence coefficients for unsteady pressure on upper surface due to oscillation of airfoil $n = 1$, $\bar{C}_{p_u}^1$				Influence coefficients for unsteady pressure on lower surface due to oscillation of airfoil $n = -1$, $\bar{C}_{p_l}^{-1}$		
0.120	----- -	----- -	----- -	0.120	----- -	----- -	----- -
0.250	----- -	----- -	----- -	0.250	----- -	----- -	----- -
0.374	----- -	----- -	----- -	0.374	----- -	----- -	----- -
0.500	1.204 -0.3005 <i>i</i>	1.242 -0.3774 <i>i</i>	1.274 -0.6315 <i>i</i>	0.500	-1.204 +0.3005 <i>i</i>	-1.242 +0.3774 <i>i</i>	-1.274 +0.6315 <i>i</i>
0.627	1.404 -0.3692 <i>i</i>	1.402 -0.4570 <i>i</i>	1.536 -0.9019 <i>i</i>	0.627	-1.404 +0.3692 <i>i</i>	-1.402 +0.4570 <i>i</i>	-1.536 +0.9019 <i>i</i>
0.750	1.067 -0.2937 <i>i</i>	1.078 -0.3751 <i>i</i>	1.037 -0.5857 <i>i</i>	0.750	-1.067 +0.2937 <i>i</i>	-1.078 +0.3751 <i>i</i>	-1.037 +0.5857 <i>i</i>
0.890	0.6880 -0.1744 <i>i</i>	0.6819 -0.2109 <i>i</i>	0.6436 -0.3052 <i>i</i>	0.890	-0.6880 +0.1744 <i>i</i>	-0.6819 +0.2109 <i>i</i>	-0.6436 +0.3052 <i>i</i>

TABLE I.—Concluded

(b) Stagger angle $\theta = 10^\circ$; runs 84 and 86; reduced frequency $k = 0.2$; Mach number $M \approx 1.95$

Ratio of streamwise coordinate to airfoil chord, x/c	Influence coefficients for unsteady pressure on lower surface due to oscillation of reference airfoil, $\bar{C}_{p_l}^0$	Influence coefficients for unsteady pressure on lower surface due to oscillation of airfoil $n = -1$, $\bar{C}_{p_l}^{-1}$	Influence coefficients for unsteady pressure on upper surface due to oscillation of reference airfoil, $\bar{C}_{p_u}^0$	Influence coefficients for unsteady pressure on upper surface due to oscillation of airfoil $n = 1$, $\bar{C}_{p_u}^1$
0.120	0.9808 -.4578 <i>i</i>	-----	-0.9686 +.5227 <i>i</i>	-----
0.250	0.8708 -.3592 <i>i</i>	-----	-0.8645 +.4130 <i>i</i>	-----
0.374	0.7964 -.3585 <i>i</i>	-0.3817 +.7019 <i>i</i>	-0.7833 +.4065 <i>i</i>	-----
0.500	1.029 -.2723 <i>i</i>	-1.201 +1.115 <i>i</i>	-0.6718 +.2735 <i>i</i>	-----
0.627	0.9671 -.3818 <i>i</i>	-1.131 +1.272 <i>i</i>	-0.9913 +.2972 <i>i</i>	1.069 -.7748 <i>i</i>
0.750	0.6473 -.1774 <i>i</i>	-0.7515 +.7654 <i>i</i>	-0.7418 +.2717 <i>i</i>	1.070 -.9695 <i>i</i>
0.890	0.4974 -.0826 <i>i</i>	-0.5506 +.4530 <i>i</i>	-1.814 +3.150 <i>i</i>	1.732 -1.576 <i>i</i>

TABLE II.—WIND TUNNEL OPERATING CONDITIONS

Data set	Stagger angle, θ , deg	Mach number, M	Average free-stream static pressure, psia	Reduced frequency, k
68	0	1.9446	7.2988	0.0562
69	0	1.9573	6.7356	.0929
77	0	1.9617	5.7019	.146
84	10	1.9477	6.2651	.200
86	-10	1.9587	6.2266	.190

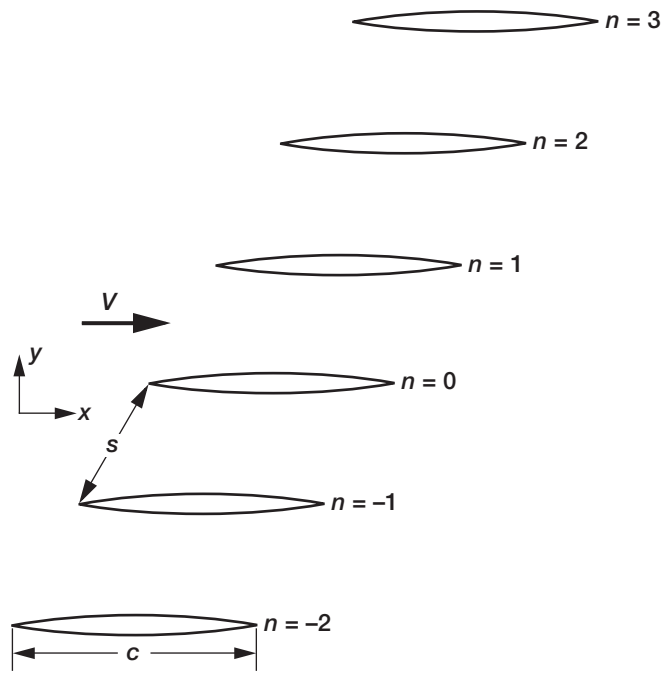


Figure 1.—Cascade of airfoils.

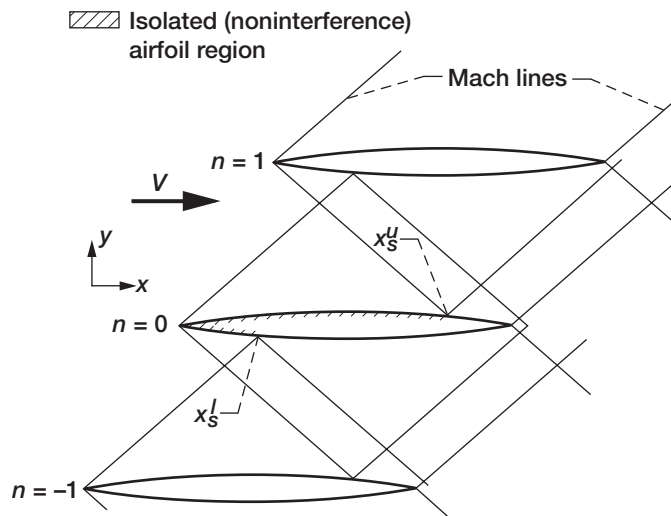


Figure 2.—Cascade of airfoils with supersonic leading-edge locus (SLEL).

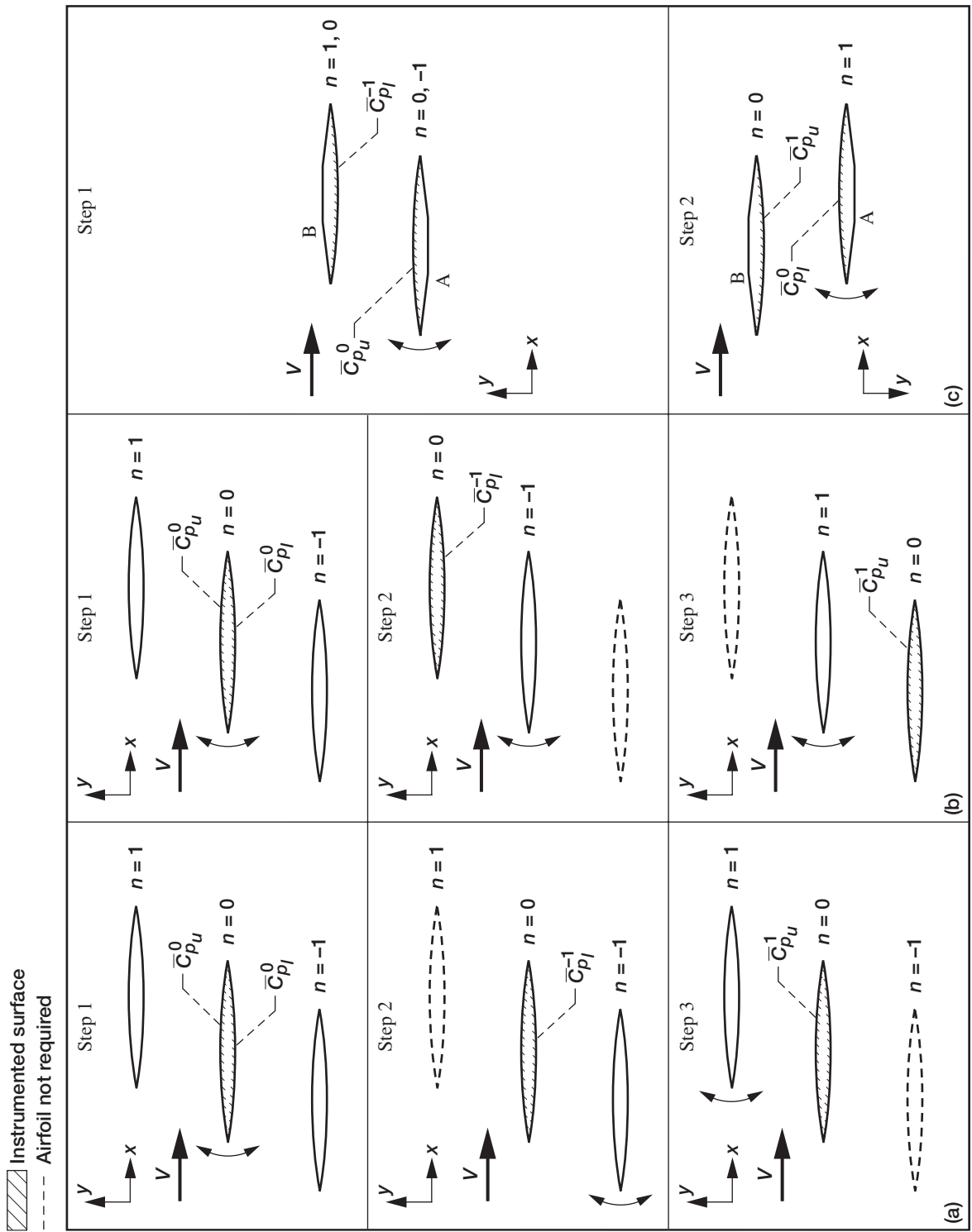


Figure 3.—Comparison of three-airfoil and two-airfoil techniques.

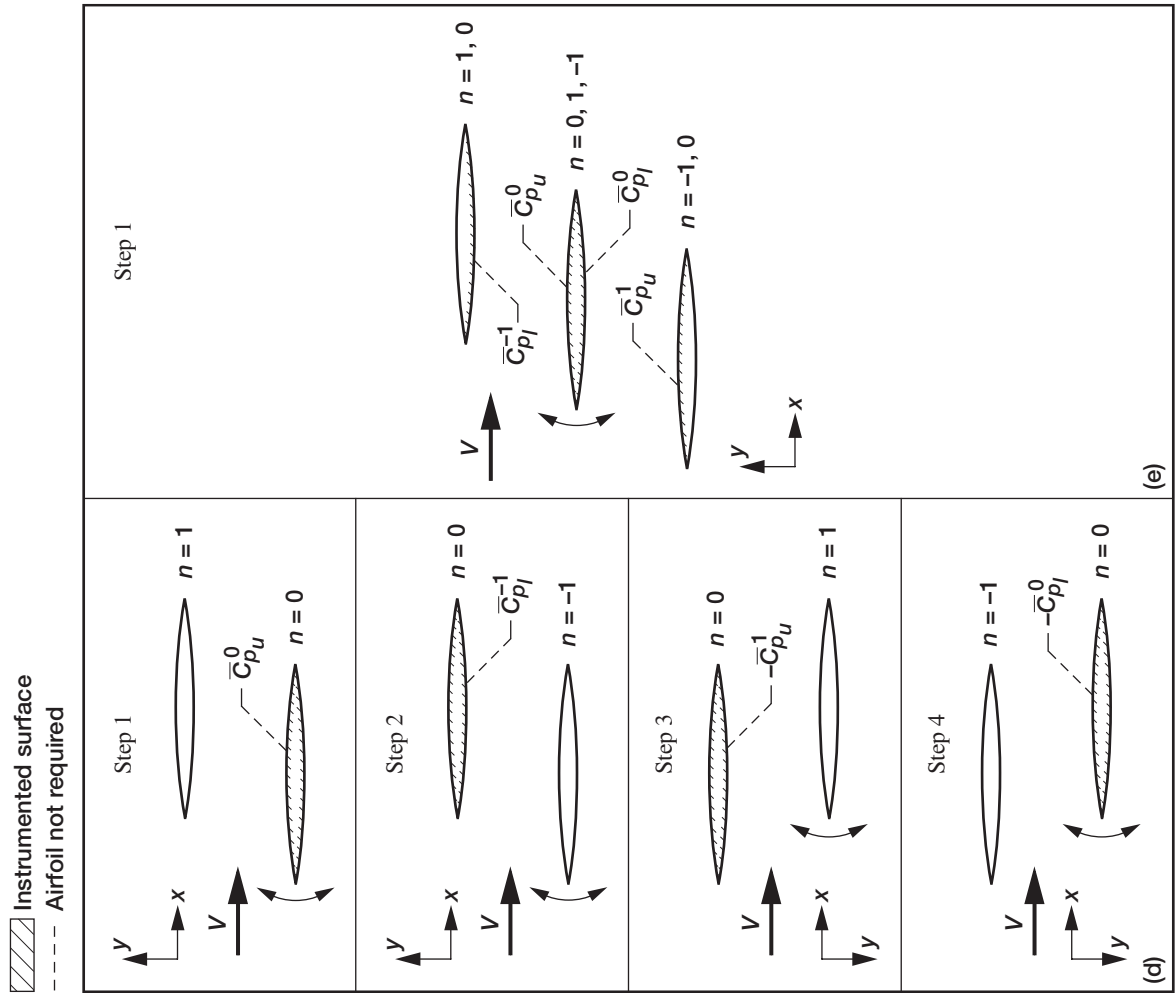


Figure 3.—Concluded. Comparison of three-airfoil and two-airfoil techniques.

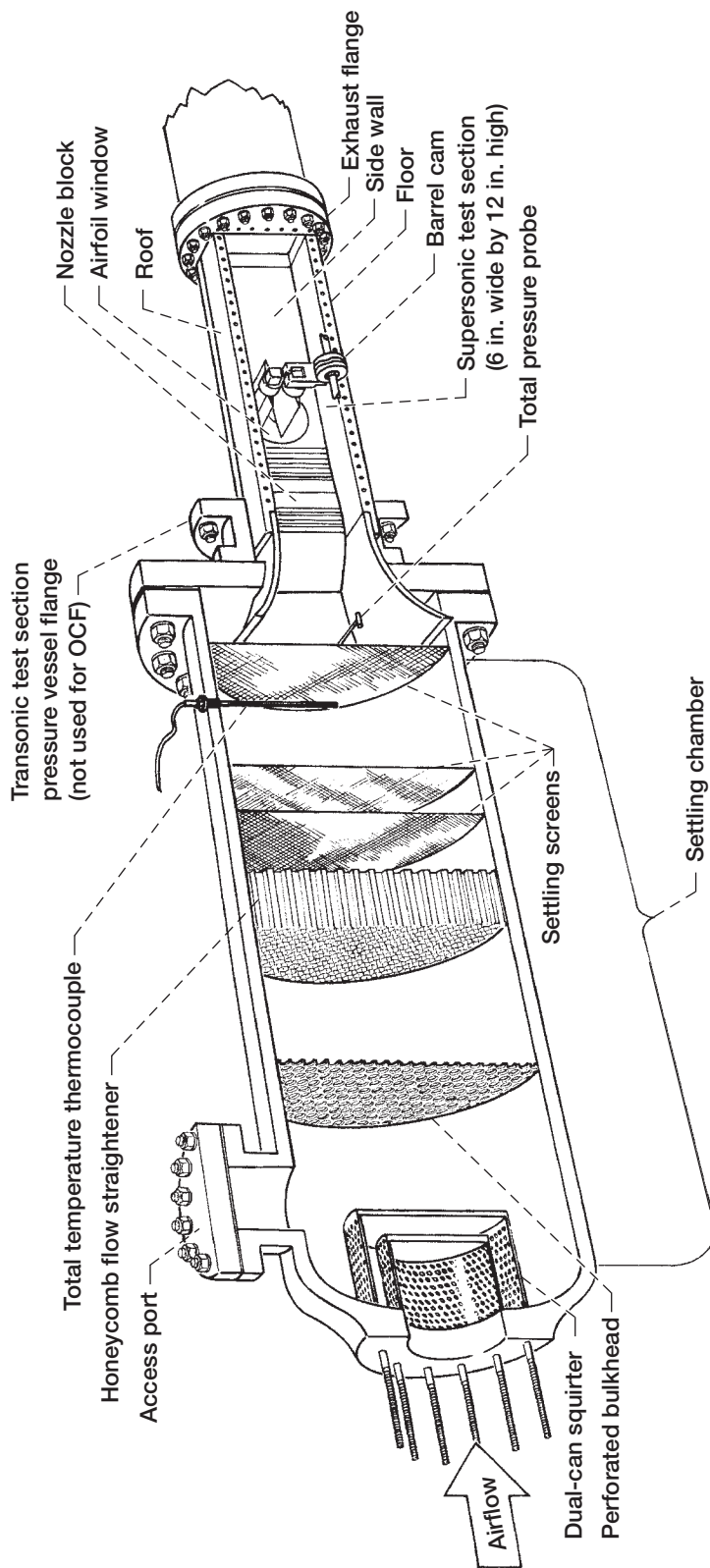


Figure 4.—Oscillating cascade facility (OCF). Click this caption in the online PDF version to view a movie of a typical wind tunnel run with an oscillating mechanism.

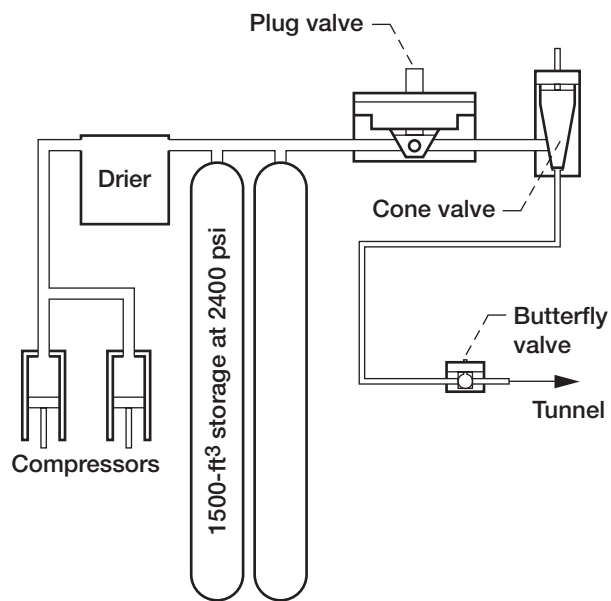


Figure 5.—Air supply for OCF.

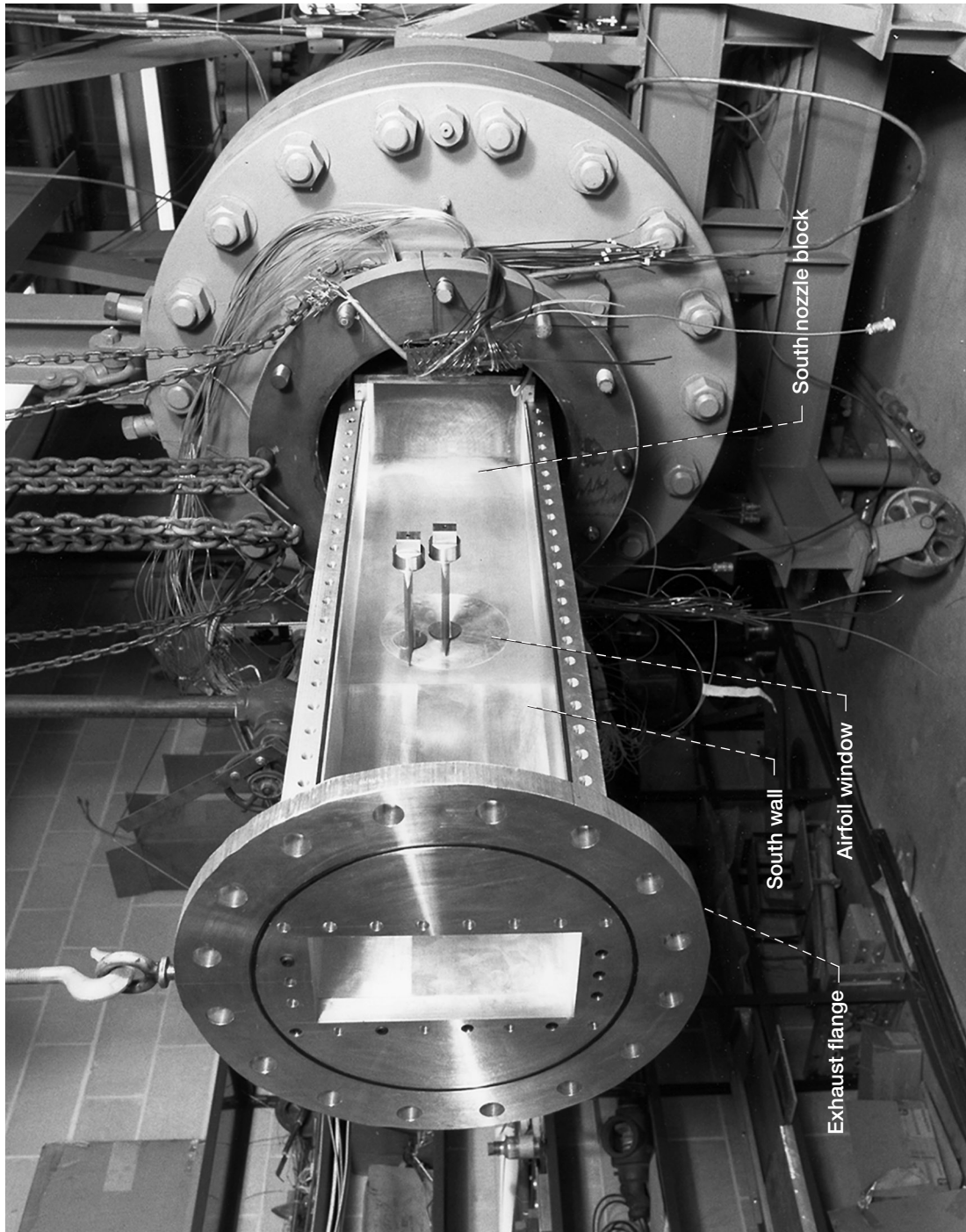


Figure 6.—OCF test section with north wall and north nozzle block removed.

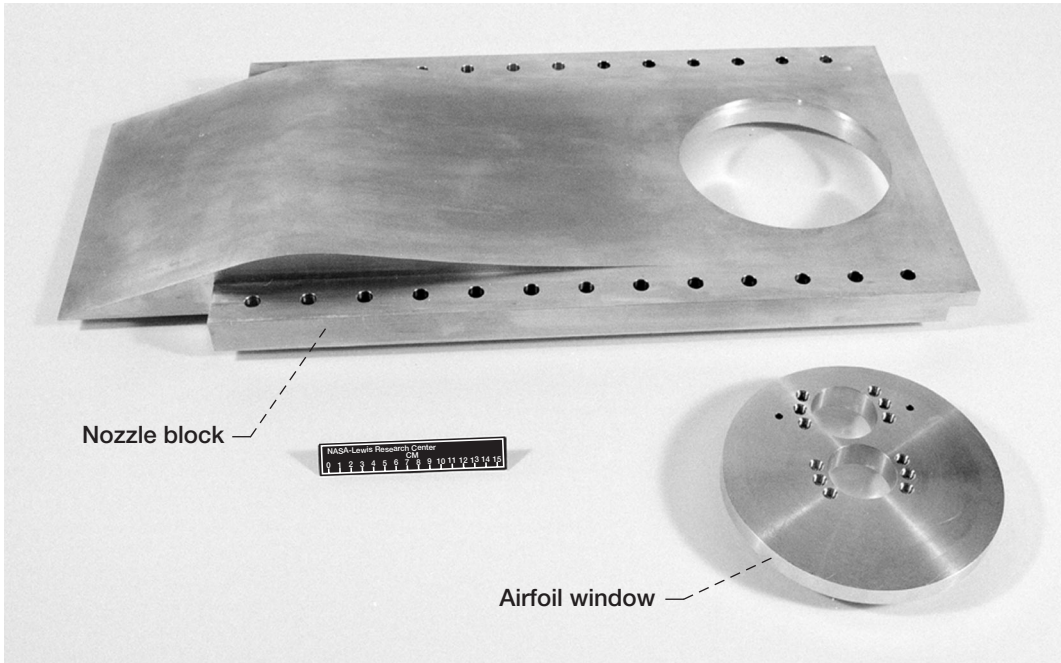


Figure 7.—Nozzle block and airfoil window.

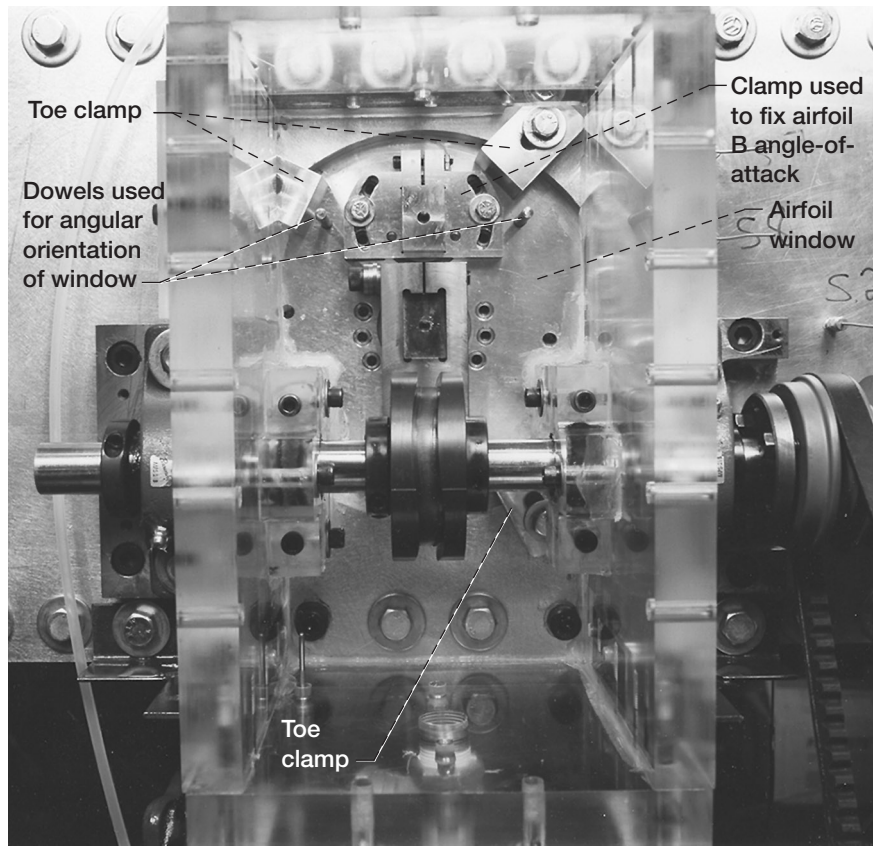


Figure 8.—Airfoil oscillating mechanism. Click this caption in the online PDF version to view a movie of a typical wind tunnel run with an oscillating mechanism.

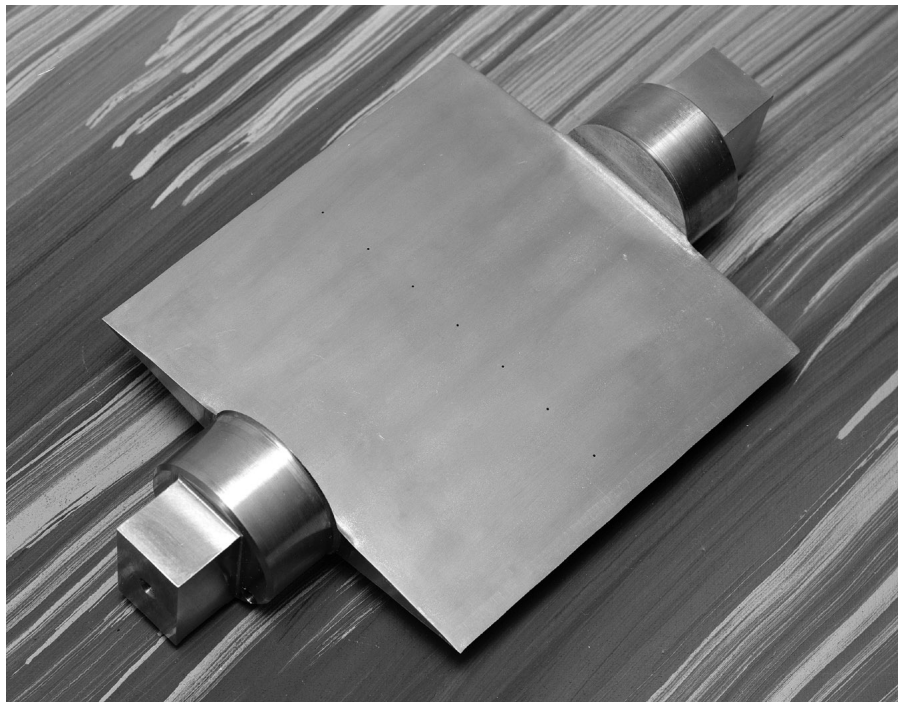


Figure 9.—Monoconvex airfoil.

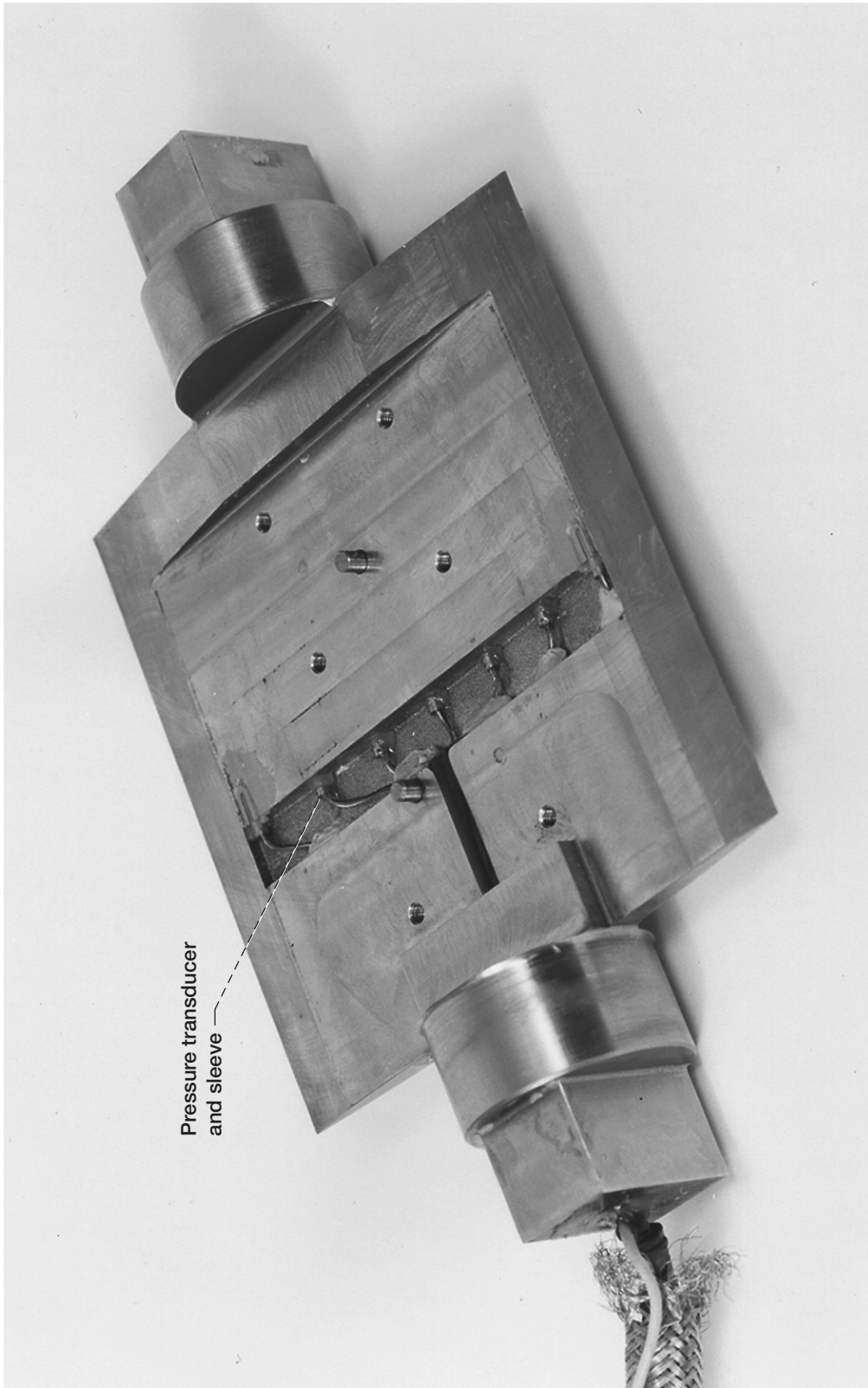


Figure 10.—Cascade airfoil with instrumentation cover removed, showing seven unsteady pressure transducers installed.



Figure 11.—Outer surface of airfoil, showing instrumentation cover installed.

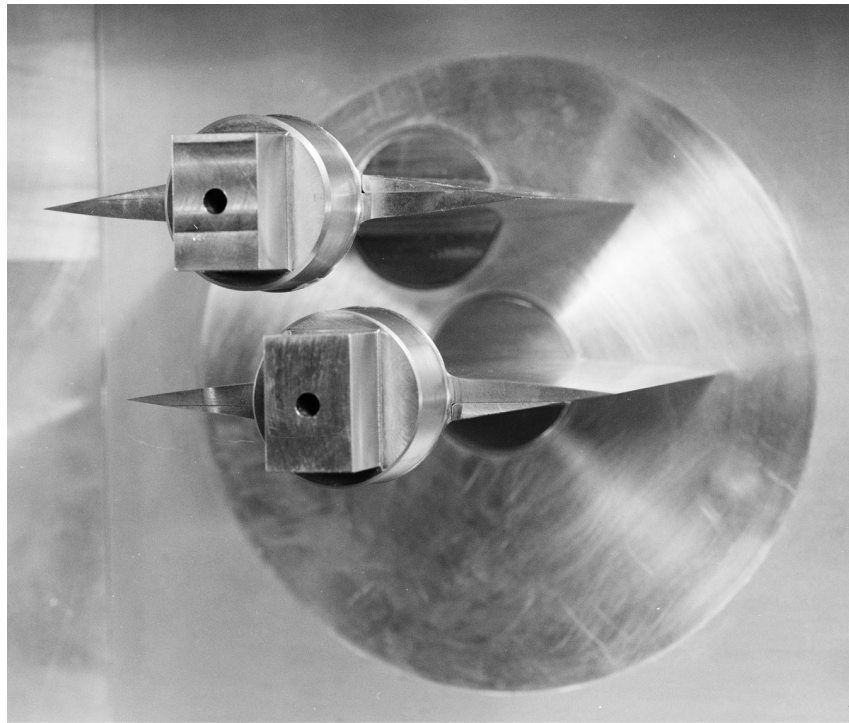
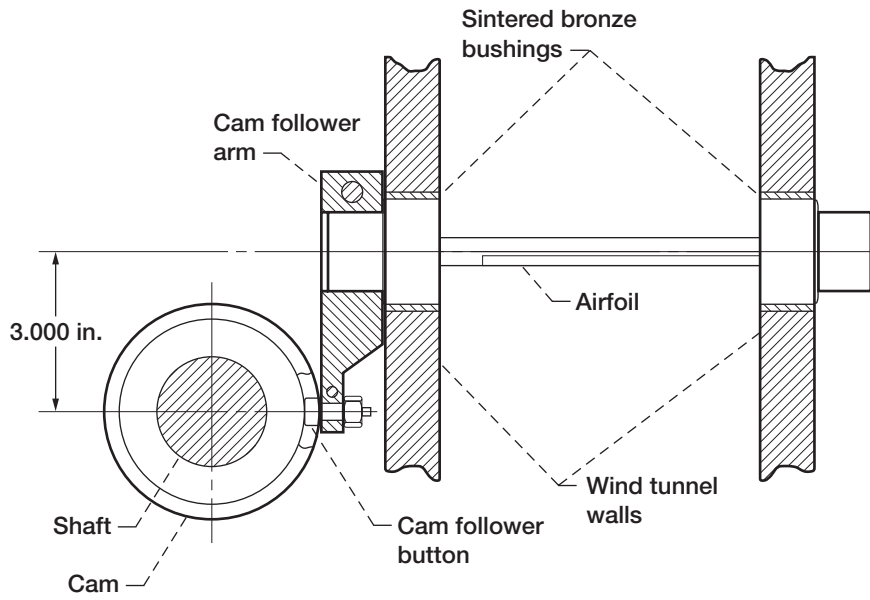
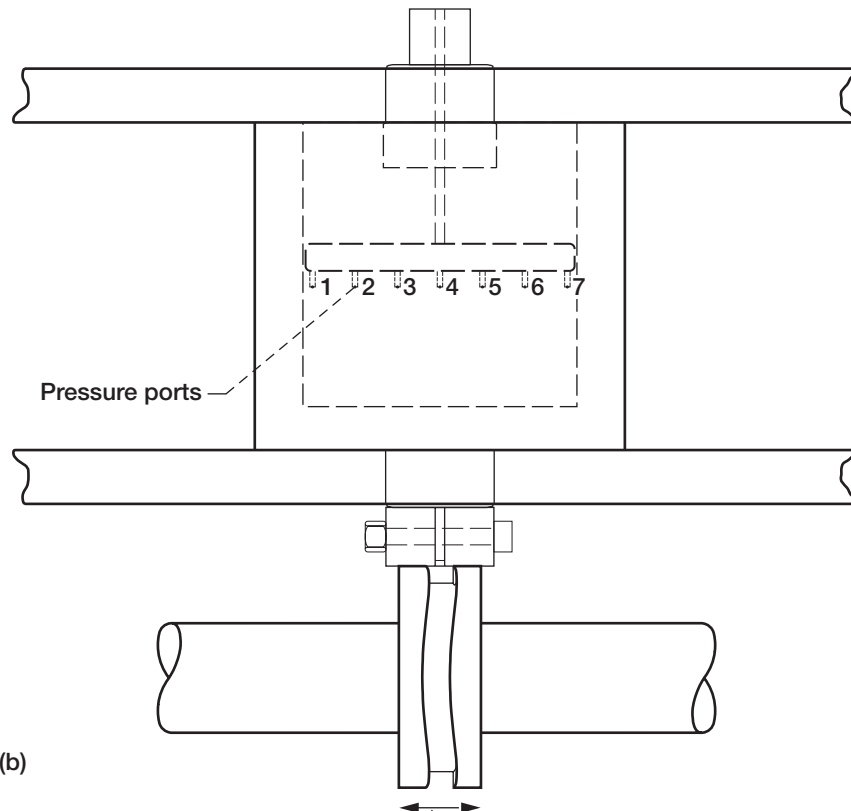


Figure 12.—Supersonic cascade.



(a)



Position of cam longitudinally on shaft will provide adjustment of airfoil mean angle of attack about which it oscillates

Figure 13.—Oscillating mechanism design. (a) View looking toward stagnation chamber. (b) Top view.

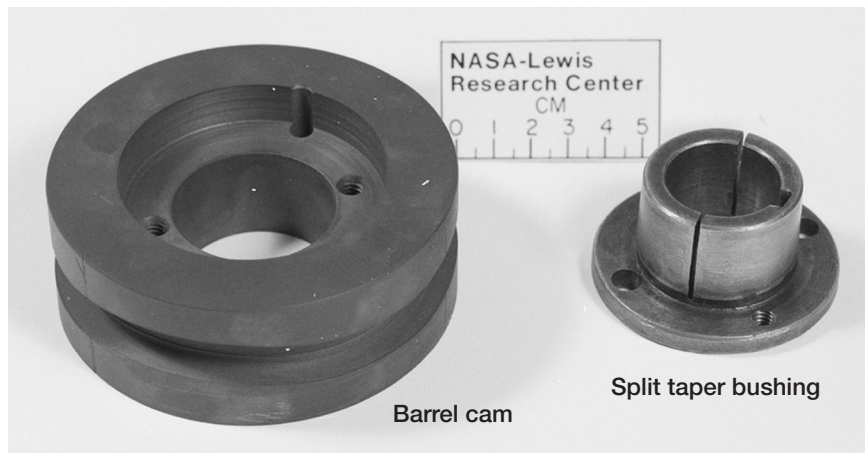


Figure 14.—Barrel cam with three-cycle-per-revolution sinusoidal groove.

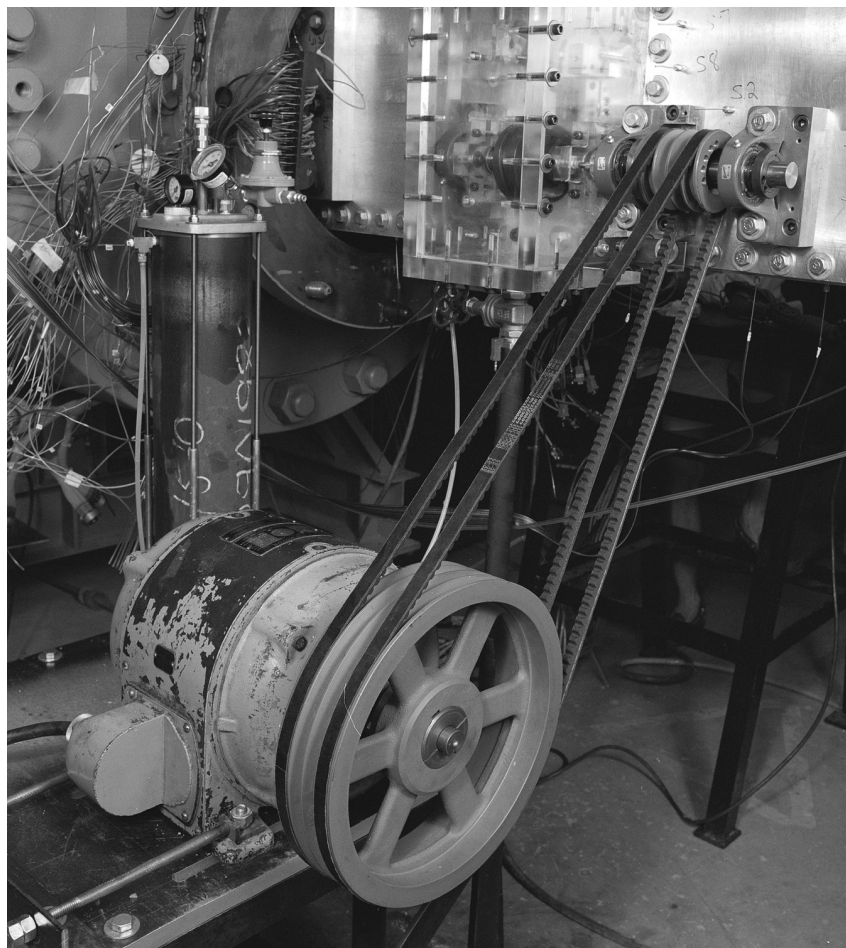


Figure 15.—Oscillating mechanism assembly.

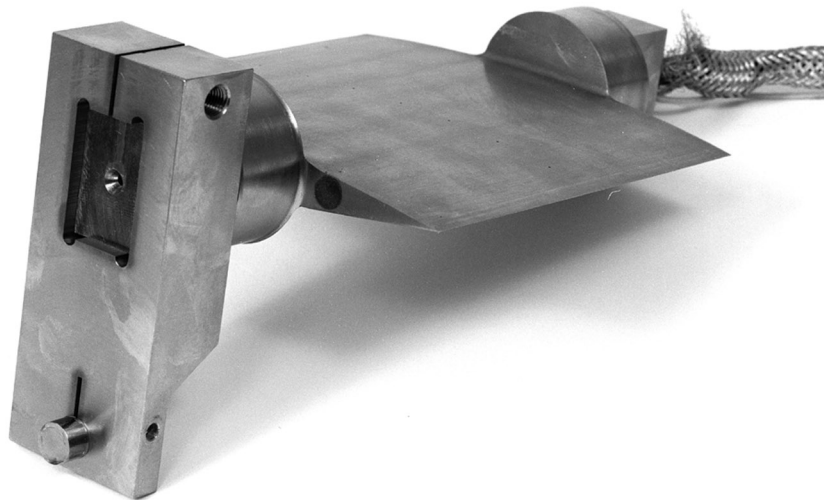


Figure 16.—Cascade airfoil, showing assembly of follower arm and cam follower button.

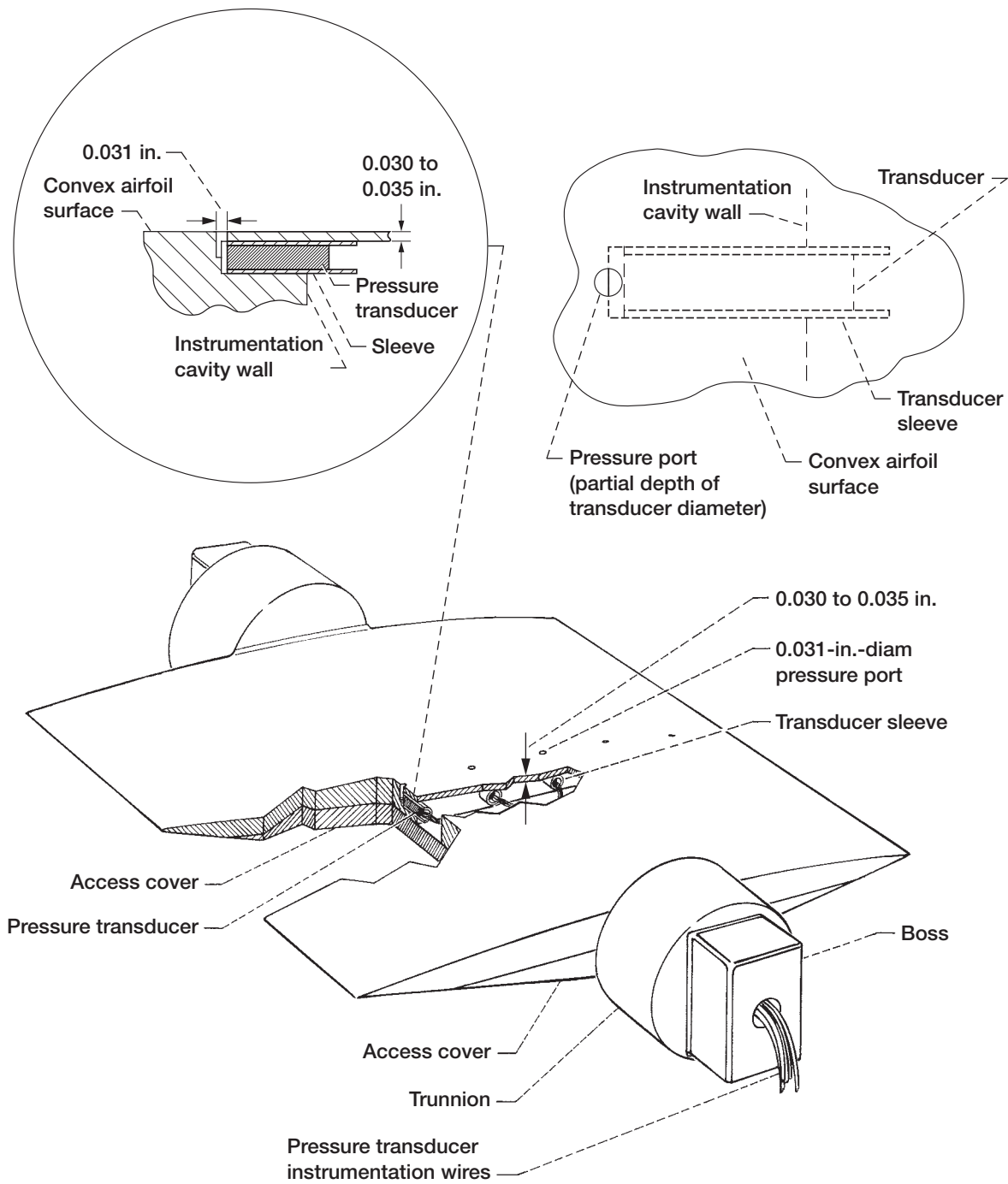


Figure 17.—Airfoil instrumentation design.

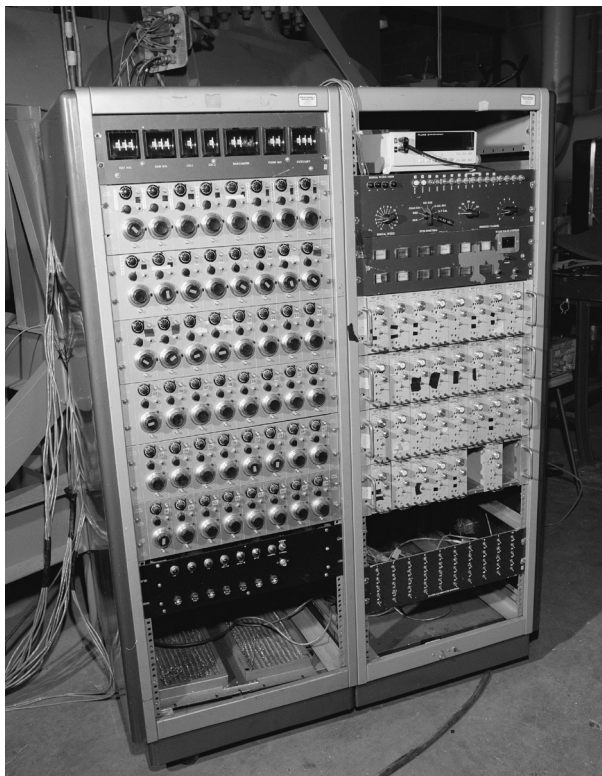


Figure 18.—Conditioning units for Kulite pressure transducers and Endevco accelerometer. (Voltage excitation and bridge-balancing units are located in left rack. Signal amplification and filtering units are located in right rack.)

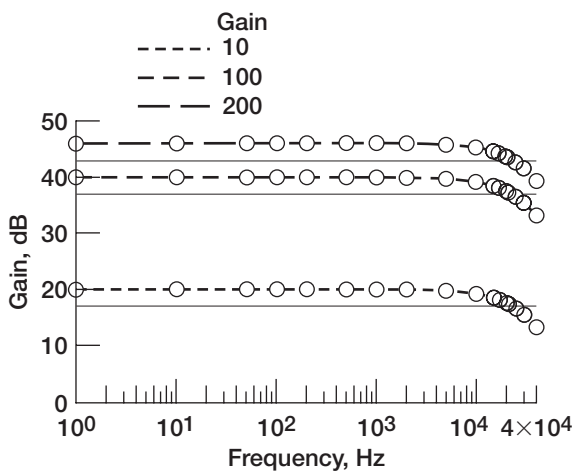


Figure 19.—Typical amplifier calibration curve.

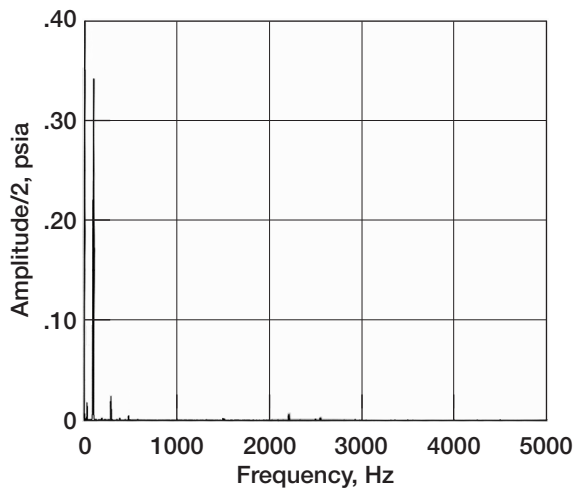


Figure 20.—Typical unsteady pressure amplitude spectrum.

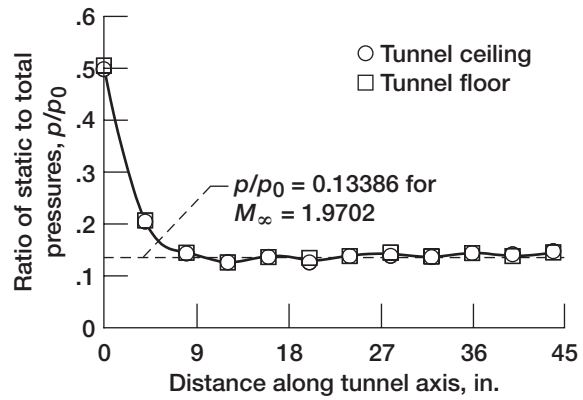


Figure 21.—Static pressure distribution for run 16. Free-stream Mach number $M_\infty = 1.9702$.

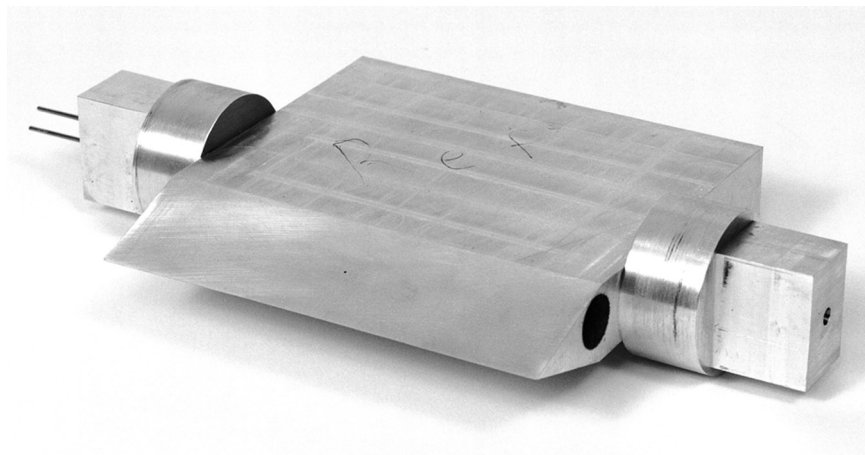


Figure 22.—Flow angle wedge.

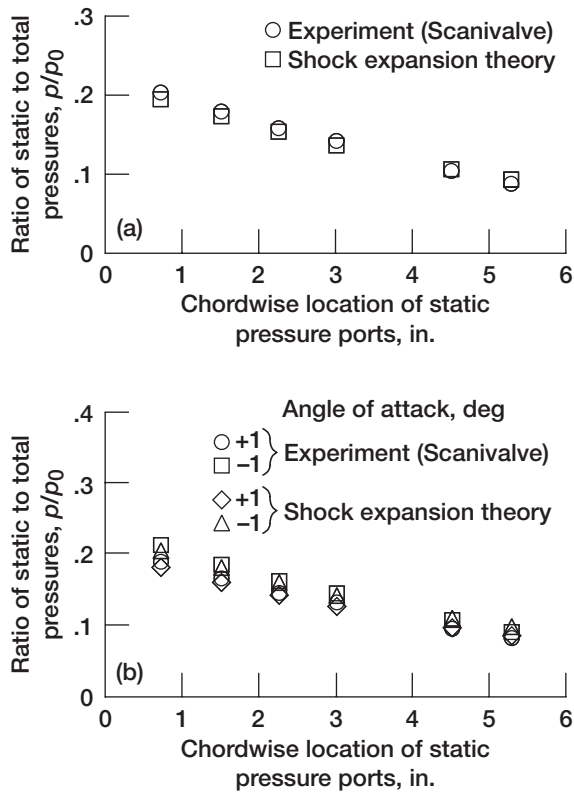


Figure 23.—Steady-state surface pressures for airfoil A at Mach 1.97. (a) 0° angle of attack. (b) $\pm 1^\circ$ angle of attack.

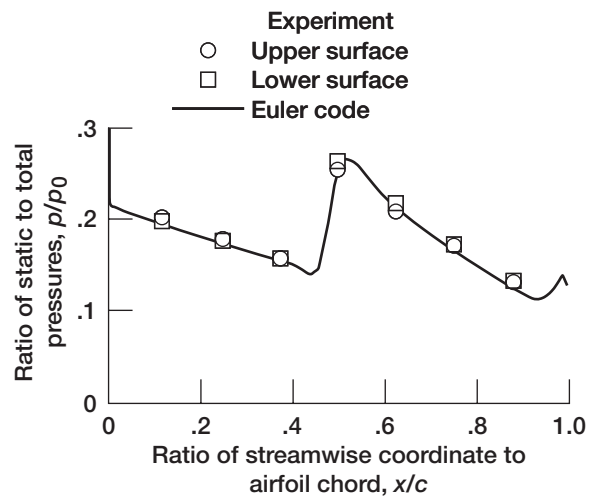


Figure 24.—Steady-state surface pressures for cascade at 0° stagger angle and Mach 1.9587.

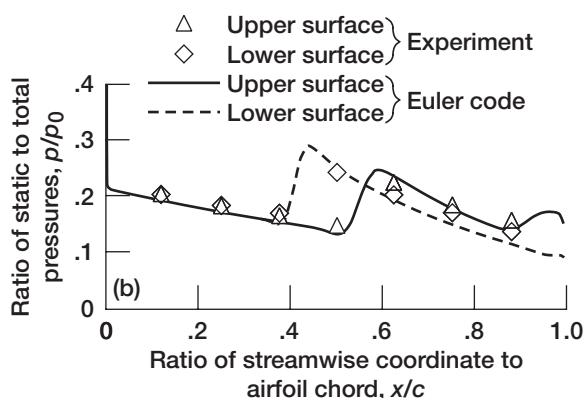
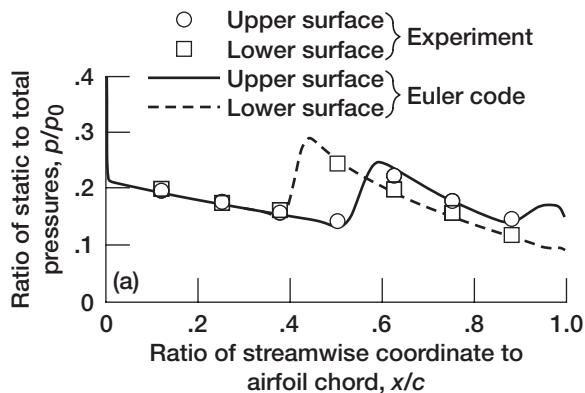


Figure 25.—Steady-state surface pressures for cascade at 10° stagger angle (free-stream Mach number $M_\infty = 1.97$; ratio of blade spacing to airfoil chord $s/c = 0.417$). (a) With Scanivalve system. (b) With Kulite transducers.

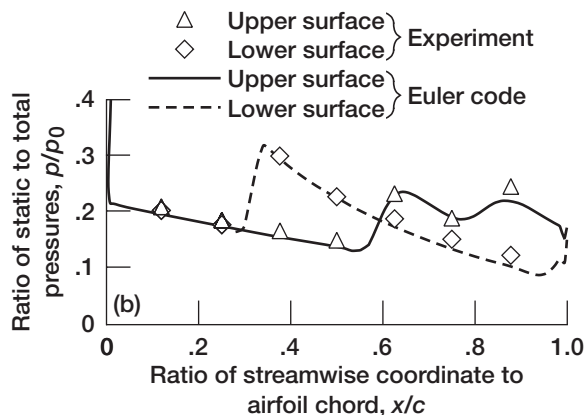
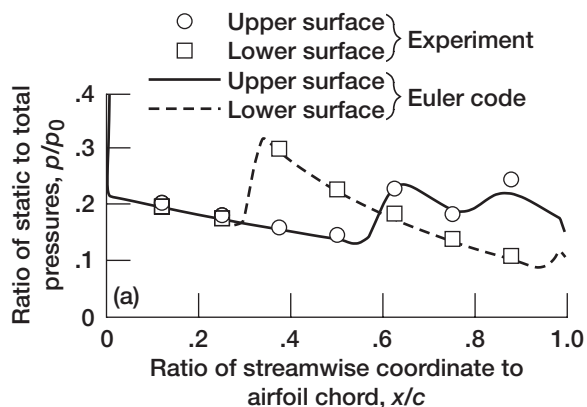


Figure 26.—Steady-state surface pressures for cascade at 20° stagger angle (free-stream Mach number $M_\infty = 1.96$; ratio of blade spacing to airfoil chord $s/c = 0.417$). (a) With Scanivalve system. (b) With Kulite transducers.

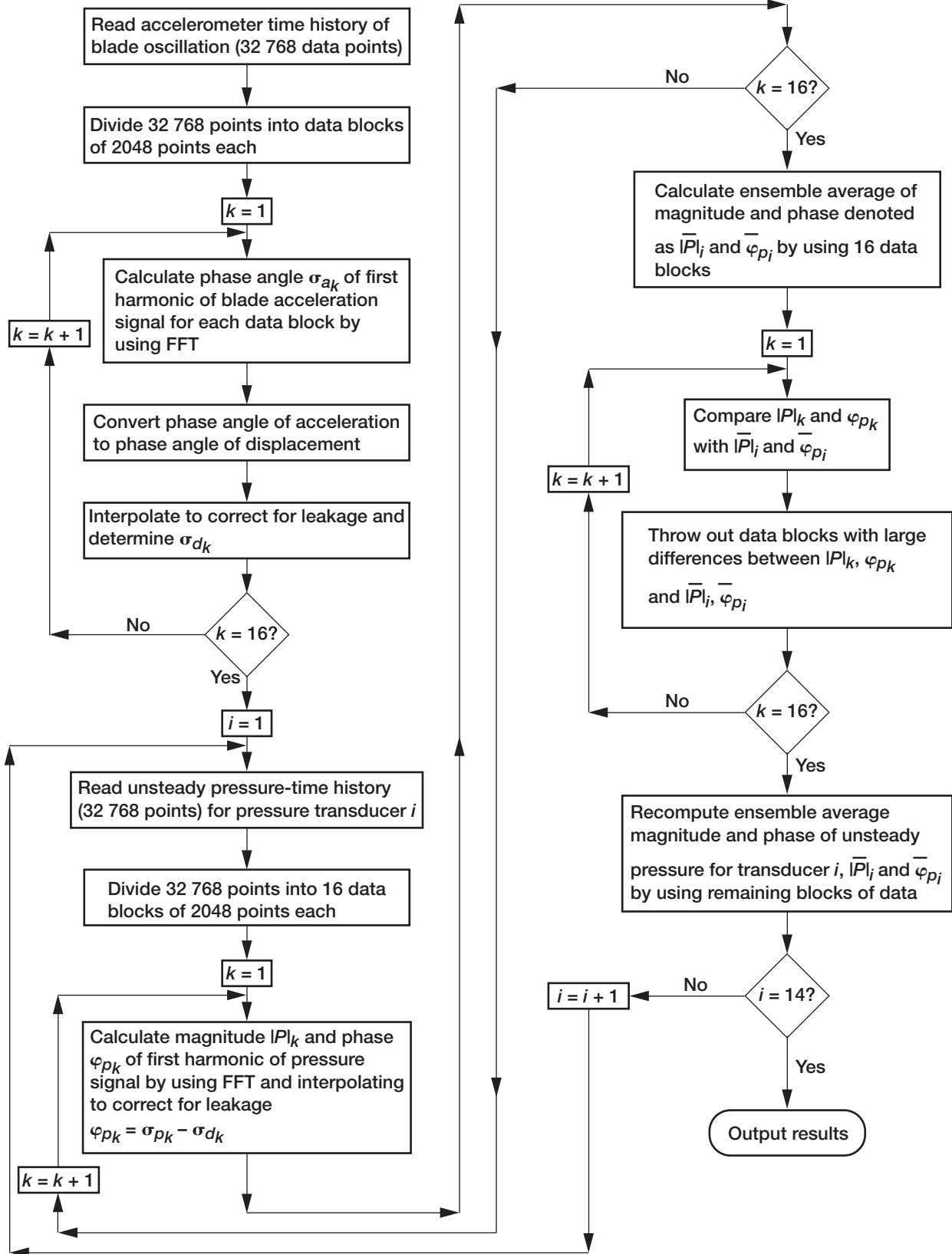


Figure 27.—Process of transforming transducer time histories into magnitude and phase (e.g., 32 768 data points assumed here).

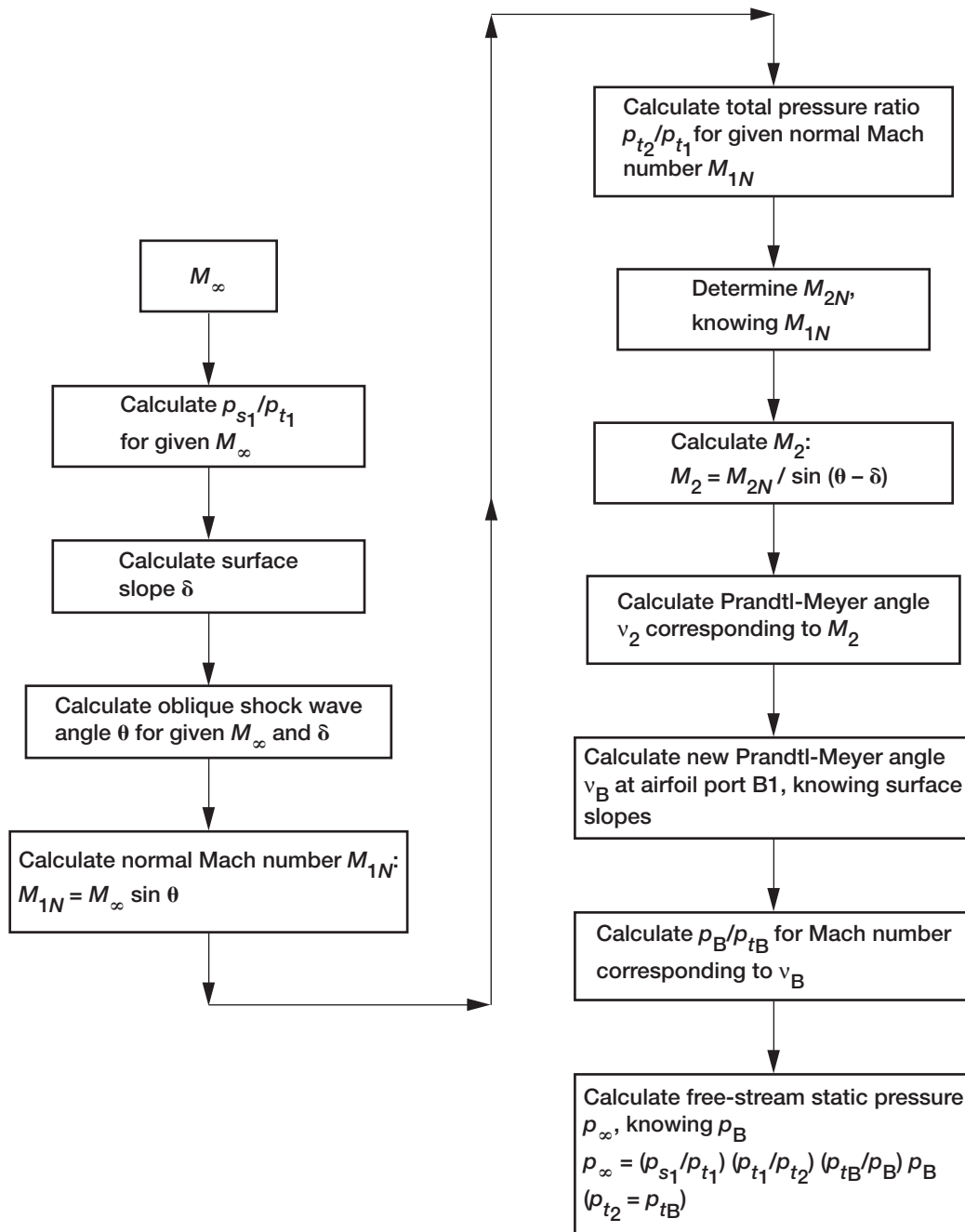


Figure 28.—Process for calculating free-stream static pressure.

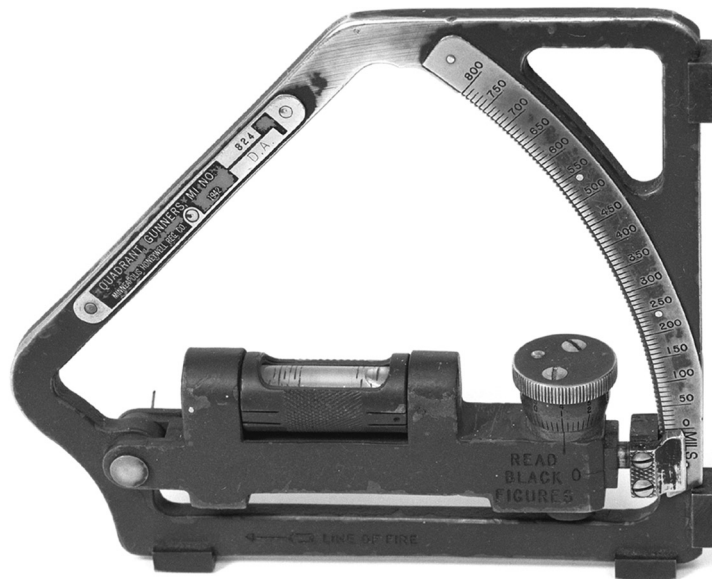


Figure 29.—Gunnery sight.

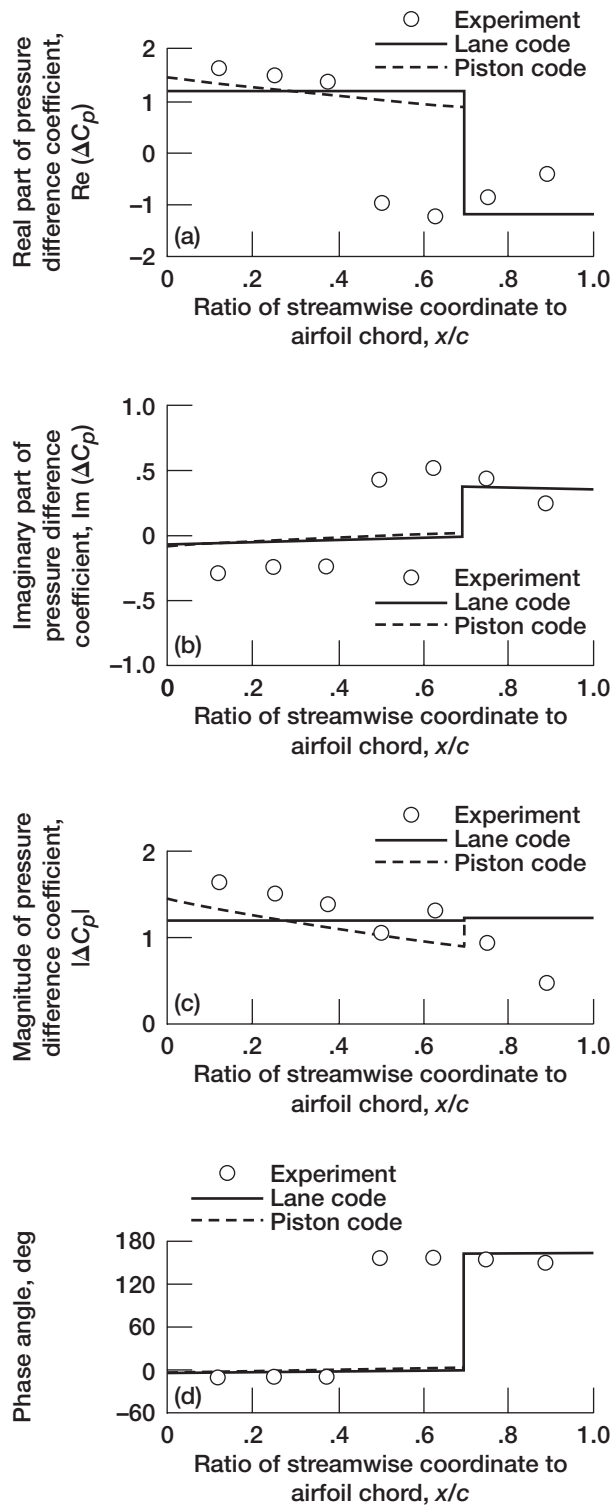


Figure 30.—Unsteady pressure difference for run 68 with interblade phase angle $\beta = 0^\circ$ (reduced frequency $k = 0.0562$; stagger angle $\theta = 0^\circ$; free-stream Mach number $M_\infty = 1.9446$; ratio of blade spacing to airfoil chord $s/c = 0.417$). (a) Real part. (b) Imaginary part. (c) Magnitude. (d) Phase angle.

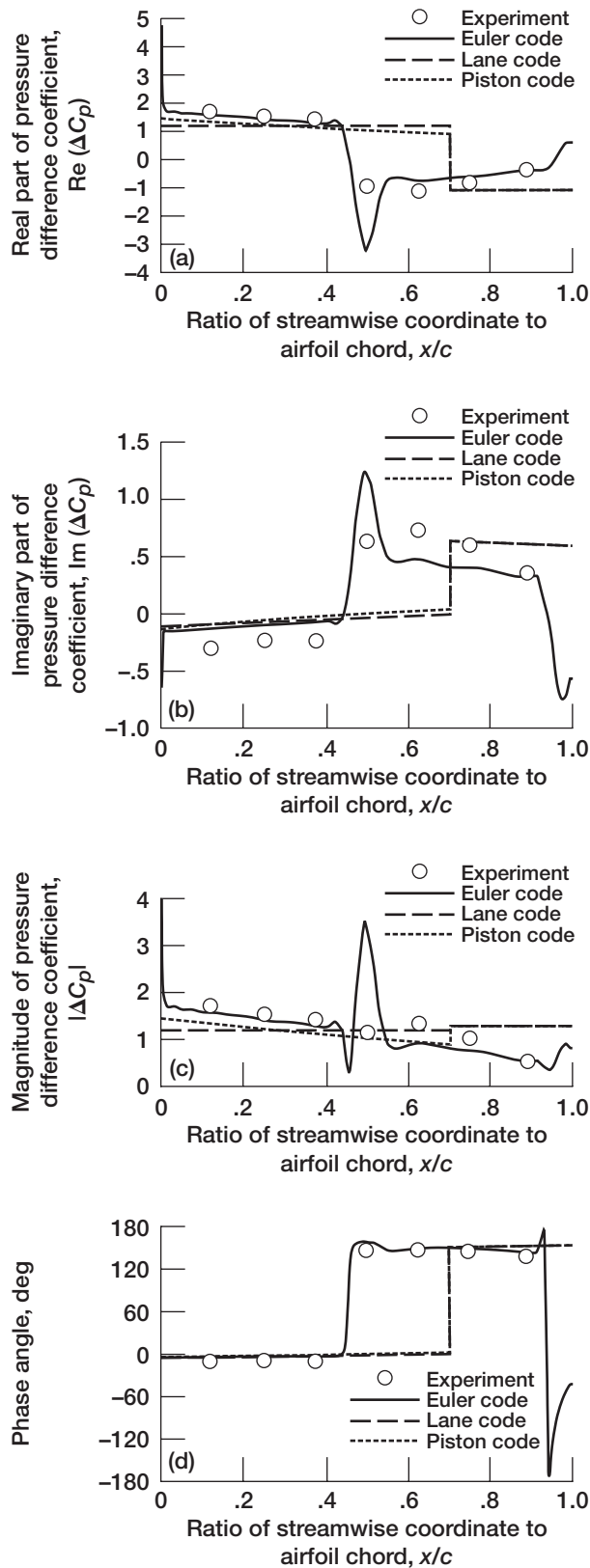


Figure 31.—Unsteady pressure difference for run 69 with interblade phase angle $\beta = 0^\circ$ (reduced frequency $k = 0.09288$; stagger angle $\theta = 0^\circ$; free-stream Mach number $M_\infty = 1.9573$; ratio of blade spacing to airfoil chord $s/c = 0.417$). (a) Real part. (b) Imaginary part. (c) Magnitude. (d) Phase angle.

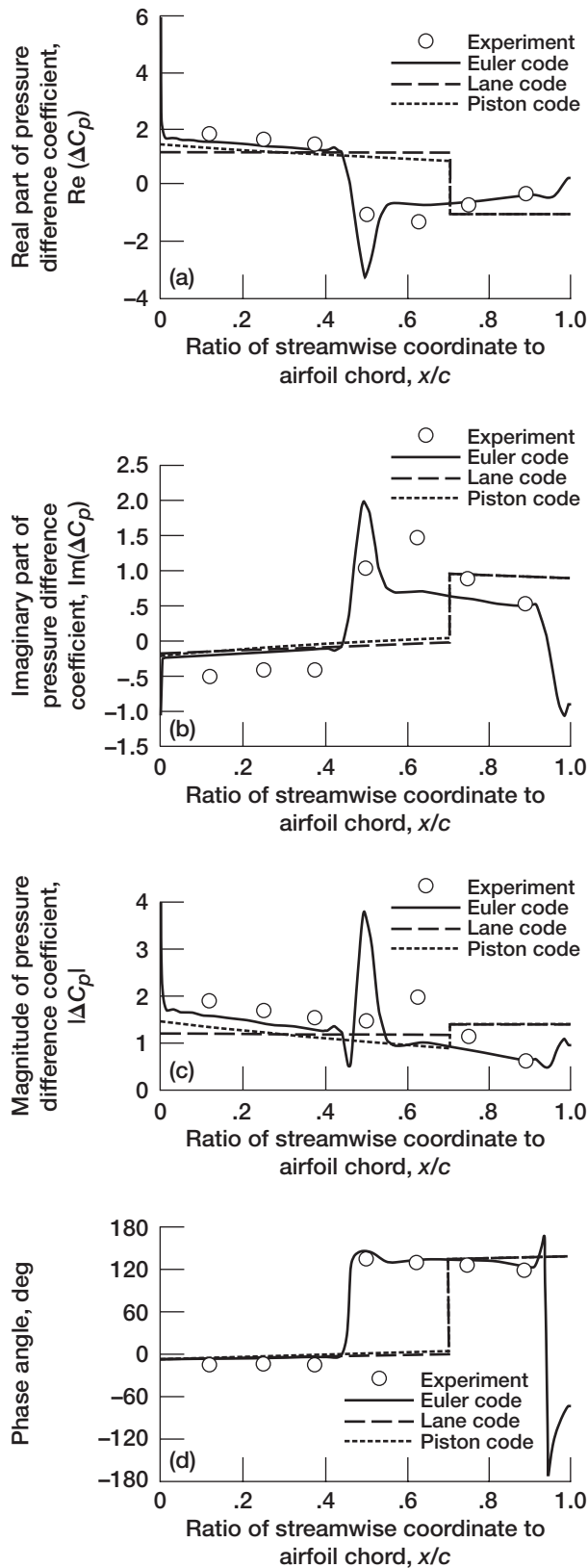
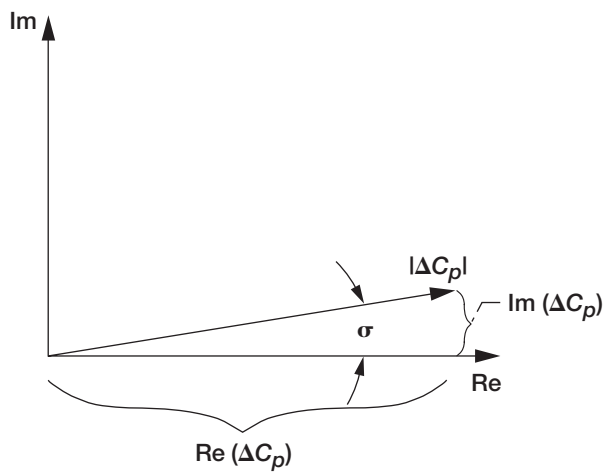


Figure 32.—Unsteady pressure difference for run 77 with interblade phase angle $\beta = 0^\circ$ (reduced frequency $k = 0.14577$; stagger angle $\theta = 0^\circ$; free-stream Mach number $M_\infty = 1.9617$; ratio of blade spacing to airfoil chord $s/c = 0.417$). (a) Real part. (b) Imaginary part. (c) Magnitude. (d) Phase angle.



$$|\Delta C_p| \cos \sigma = \text{Re}(\Delta C_p)$$

$$|\Delta C_p| \sin \sigma \cong |\Delta C_p| \sigma = \text{Im}(\Delta C_p)$$

Figure 33.—Effects of phase angle error. (Assume that $\sigma_{\text{correct}} = 10^\circ$. If σ_{measured} is 5° (50 percent off), then $\text{Im}(\Delta C_p)$ will be 50 percent off. However, $\text{Re}(\Delta C_p)$ will only be 1.15 percent off, since $\cos(10^\circ) = 0.98481$ and $\cos(5^\circ) = 0.99619$.)

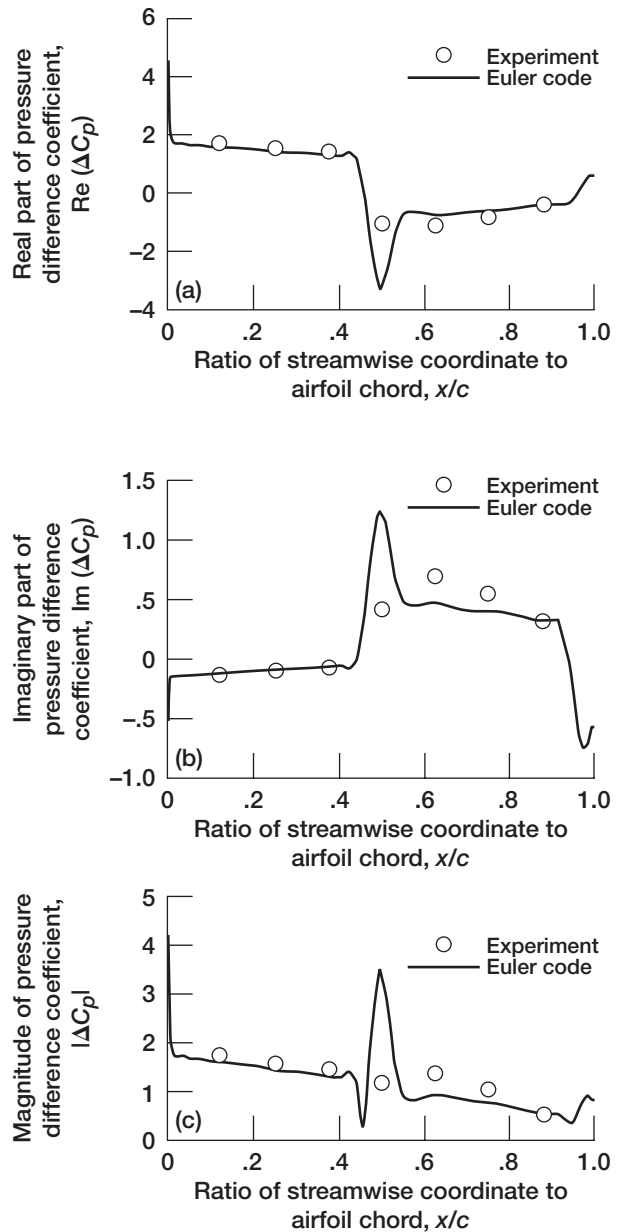


Figure 34.—Unsteady pressure difference for run 69 using phase angles from Euler code (reduced frequency $k = 0.09288$; interblade phase angle $\beta = 0^\circ$; stagger angle $\theta = 0^\circ$; free-stream Mach number $M_\infty = 1.9573$; ratio of blade spacing to airfoil chord $s/c = 0.417$). (a) Real part. (b) Imaginary part. (c) Magnitude.

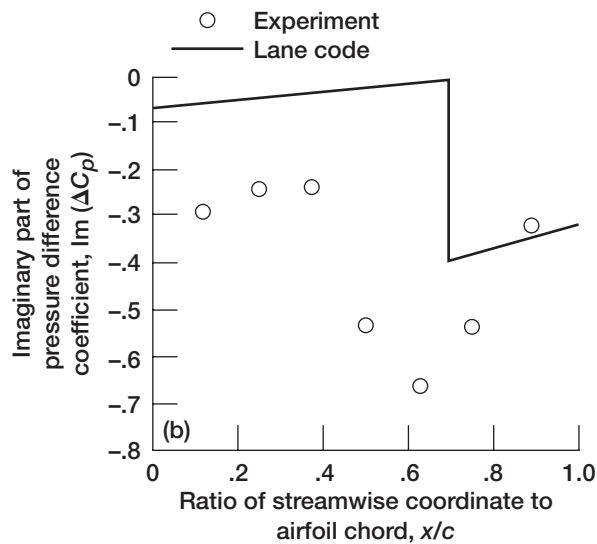
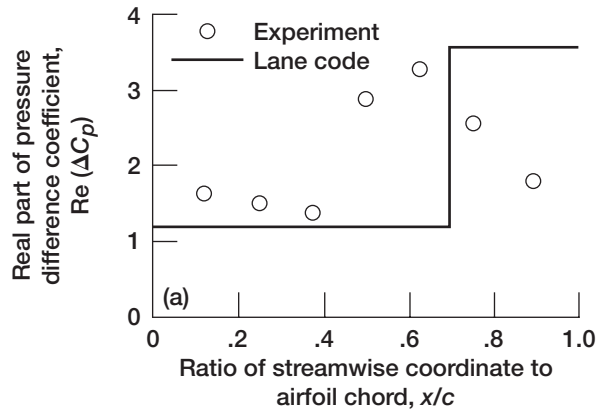


Figure 35.—Unsteady pressure difference for run 68 with interblade phase angle $\beta = 180^\circ$ (reduced frequency $k = 0.0562$; stagger angle $\theta = 0^\circ$; free-stream Mach number $M_\infty = 1.9446$; ratio of blade spacing to airfoil chord $s/c = 0.417$). (a) Real part. (b) Imaginary part.

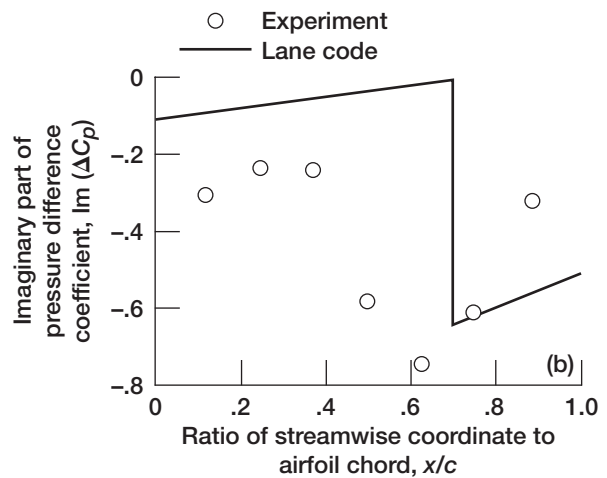
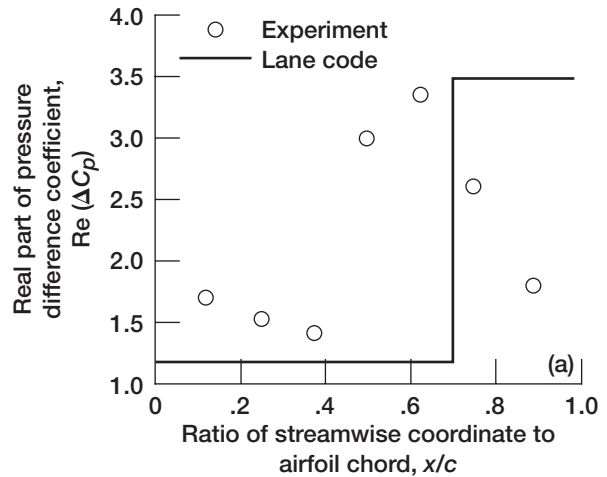


Figure 36.—Unsteady pressure difference for run 69 with interblade phase angle $\beta = 180^\circ$ (reduced frequency $k = 0.09288$; stagger angle $\theta = 0^\circ$; free-stream Mach number $M_\infty = 1.9573$; ratio of blade spacing to airfoil chord $s/c = 0.417$). (a) Real part. (b) Imaginary part.

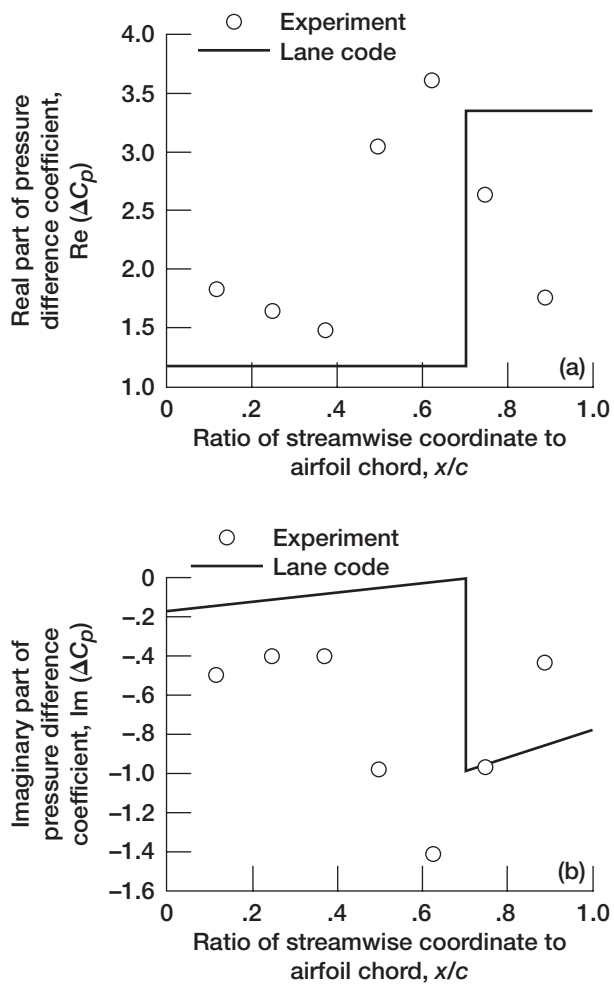


Figure 37.—Unsteady pressure difference for run 77 with interblade phase angle $\beta = 180^\circ$ (reduced frequency $k = 0.14577$; stagger angle $\theta = 0^\circ$; free-stream Mach number $M_\infty = 1.9617$; ratio of blade spacing to airfoil chord $s/c = 0.417$). (a) Real part. (b) Imaginary part.

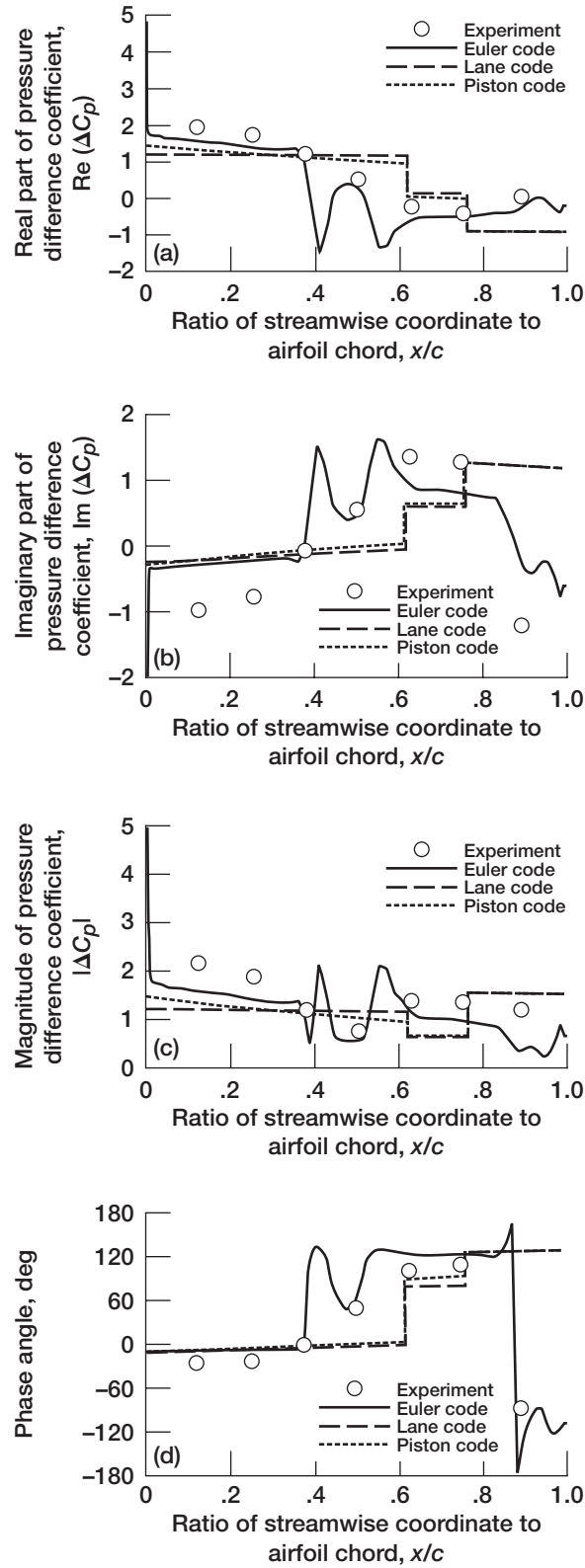


Figure 38.—Unsteady pressure difference for runs 84 and 86 with interblade phase angle $\beta = 0^\circ$ and stagger angle $\theta = 10^\circ$ (reduced frequency $k = 0.2$; free-stream Mach number $M_\infty = 1.9532$; ratio of blade spacing to airfoil chord $s/c = 0.417$). (a) Real part. (b) Imaginary part. (c) Magnitude. (d) Phase angle.

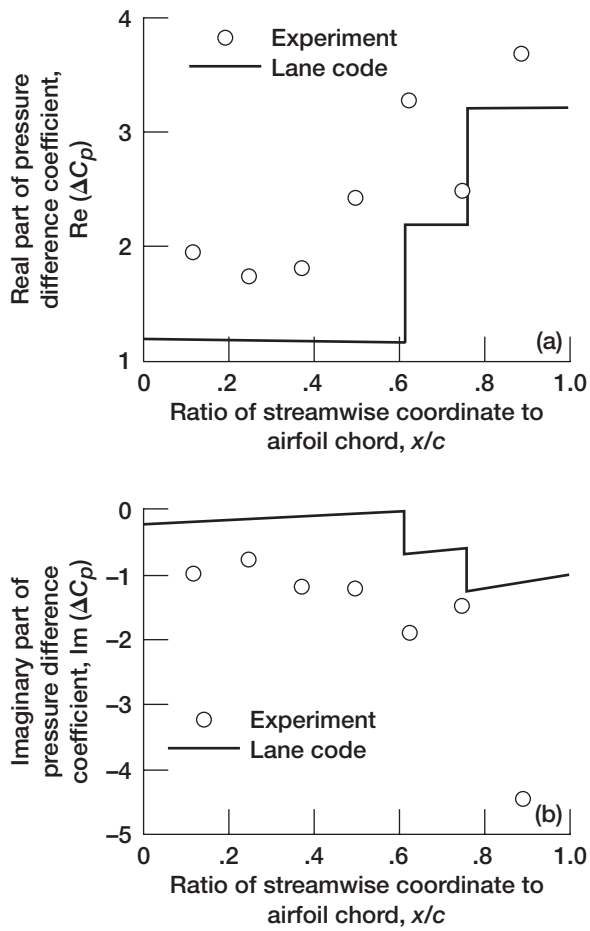


Figure 39.—Unsteady pressure difference for runs 84 and 86 with interblade phase angle $\beta = 180^\circ$ and stagger angle $\theta = 10^\circ$ (reduced frequency $k = 0.2$; free-stream Mach number $M_\infty = 1.9532$; ratio of blade spacing to airfoil chord $s/c = 0.417$). (a) Real part. (b) Imaginary part.

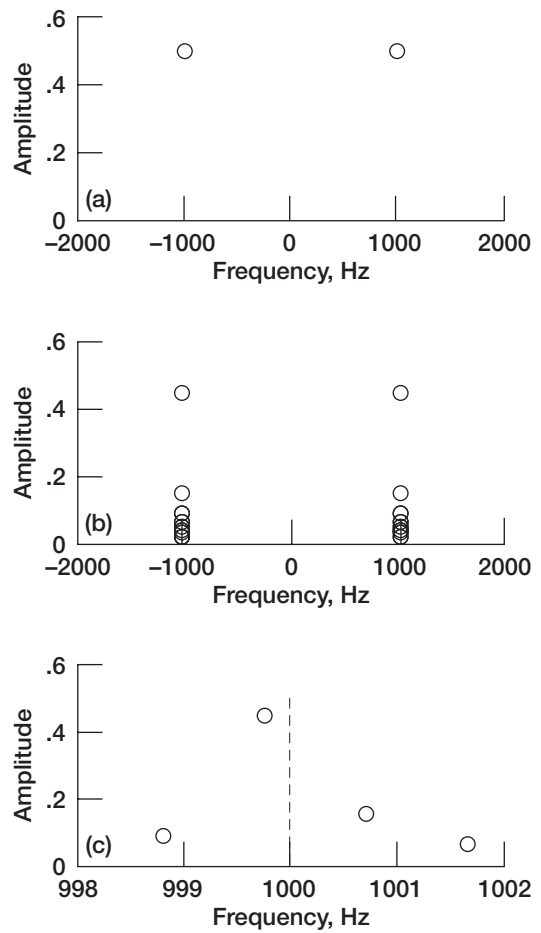


Figure 40.—Frequency spectrum of continuous cosine wave of amplitude 1 and frequency of 1000 Hz using rectangular data window. (a) Integer number of cycles in data window. (b) Noninteger number of cycles in data window. (c) Detailed view of (b).

REPORT DOCUMENTATION PAGE

Form Approved
OMB No. 0704-0188

Public reporting burden for this collection of information is estimated to average 1 hour per response, including the time for reviewing instructions, searching existing data sources, gathering and maintaining the data needed, and completing and reviewing the collection of information. Send comments regarding this burden estimate or any other aspect of this collection of information, including suggestions for reducing this burden, to Washington Headquarters Services, Directorate for Information Operations and Reports, 1215 Jefferson Davis Highway, Suite 1204, Arlington, VA 22202-4302, and to the Office of Management and Budget, Paperwork Reduction Project (0704-0188), Washington, DC 20503.

1. AGENCY USE ONLY (<i>Leave blank</i>)		2. REPORT DATE June 2004	3. REPORT TYPE AND DATES COVERED Technical Memorandum	
4. TITLE AND SUBTITLE Comparison of Theoretical and Experimental Unsteady Aerodynamics of Linear Oscillating Cascade With Supersonic Leading-Edge Locus			5. FUNDING NUMBERS WBS-22-297-10-06	
6. AUTHOR(S) John K. Ramsey and Dan Erwin				
7. PERFORMING ORGANIZATION NAME(S) AND ADDRESS(ES) National Aeronautics and Space Administration John H. Glenn Research Center at Lewis Field Cleveland, Ohio 44135-3191			8. PERFORMING ORGANIZATION REPORT NUMBER E-13512	
9. SPONSORING/MONITORING AGENCY NAME(S) AND ADDRESS(ES) National Aeronautics and Space Administration Washington, DC 20546-0001			10. SPONSORING/MONITORING AGENCY REPORT NUMBER NASA TM-2004-211820	
11. SUPPLEMENTARY NOTES John K. Ramsey, NASA Glenn Research Center, and Dan Erwin, Ohio State University, Columbus, Ohio 43210. Responsible person, John K. Ramsey, organization code 7740, 216-433-6032. The CD in the back of this report contains a PDF file of this report with links to view the movie along with the movie file of a typical wind tunnel run with an oscillating mechanism. Links to view the movie can also be found in figures 4 and 8 in the online PDF version.				
12a. DISTRIBUTION/AVAILABILITY STATEMENT Unclassified - Unlimited Subject Category: 02 Available electronically at http://gltrs.grc.nasa.gov This publication is available from the NASA Center for AeroSpace Information, 301-621-0390.			12b. DISTRIBUTION CODE	
13. ABSTRACT (<i>Maximum 200 words</i>) An experimental influence coefficient technique was used to obtain unsteady aerodynamic influence coefficients and, consequently, unsteady pressures for a cascade of symmetric airfoils oscillating in pitch about midchord. Stagger angles of 0° and 10° were investigated for a cascade with a gap-to-chord ratio of 0.417 operating at an axial Mach number of 1.9, resulting in a supersonic leading-edge locus. Reduced frequencies ranged from 0.056 to 0.2. The influence coefficients obtained determine the unsteady pressures for any interblade phase angle. The unsteady pressures were compared with those predicted by several algorithms for interblade phase angles of 0° and 180°.				
14. SUBJECT TERMS Supersonic; Unsteady aerodynamics; Cascade; Flutter; Aerodynamics; Supersonic wind tunnels; Influence coefficient			15. NUMBER OF PAGES 61	
			16. PRICE CODE	
17. SECURITY CLASSIFICATION OF REPORT Unclassified	18. SECURITY CLASSIFICATION OF THIS PAGE Unclassified	19. SECURITY CLASSIFICATION OF ABSTRACT Unclassified	20. LIMITATION OF ABSTRACT	

